PAPER • OPEN ACCESS

Evaluation of SPARC divertor conditions in H-mode operation using SOLPS-ITER

To cite this article: Jeremy D. Lore *et al* 2024 *Nucl. Fusion* **64** 126054

OPEN ACCESS
IOP Publishing | International Atomic Energy Agency
Nuclear Fusion
Nucl. Fusion **64** (2024) 126054 (17pp)
https://doi.org/10.1088/1741-4326/ad85f3

Evaluation of SPARC divertor conditions in H-mode operation using SOLPS-ITER

Jeremy D. Lore[1,*], Jae-Sun Park[1], Thomas Eich[2], Adam Q. Kuang[2], Matthew L. Reinke[2], Sebastian De Pascuale[1], Bart Lomanowski[1], Alex Creely[2] and John M. Canik[1]

[1] Oak Ridge National Laboratory, Oak Ridge, TN 37831, United States of America
[2] Commonwealth Fusion Systems, Cambridge, MA 02139, United States of America

E-mail: lorejd@ornl.gov

Received 12 August 2024, revised 20 September 2024
Accepted for publication 11 October 2024
Published 18 October 2024

Abstract

The predicted divertor conditions for the SPARC tokamak are calculated using SOLPS-ITER for a range of scrape-off-layer (SOL) heat flux widths λ_q, input powers, and particle fueling locations. Under H-mode scenario conditions with an upstream separatrix density of 1×10^{20} m^{-3}, the most conservative range of λ_q extrapolations ($\approx$0.15 mm) results in extremely high unmitigated particle and energy fluxes to the divertor, both under full field (12.2 T) and power ($P_{\mathrm{SOL}} = 29$ MW) conditions, and 2/3 field with $P_{\mathrm{SOL}} = 10$ MW. Increasing the cross-field SOL diffusivities by 2–10$\times$ reduces the magnitude of the mitigation challenge, however strategies such as impurity seeding or strike-point-sweeping will likely still be required. A combination of steady-state and time-dependent SOLPS-ITER simulations are used to map out phase space diagrams of upstream and divertor conditions. The simulations include parallel currents but neglect cross-field drifts. At low upstream density the inner and outer divertor conditions are highly asymmetric, with a large temperature difference and significant heat fluxes driven by parallel currents. The solution has sharp bifurcations with a region of hysteresis, depending on whether the initial state is at a low or high density. This behavior is observed even when the fueling location, cross-field diffusivity, and impurity level is changed, although the density window with asymmetry is reduced with increasing diffusivity. The addition of neon impurity seeding reduces the divertor heat fluxes, but also causes a drop in the upstream electron density with fixed particle throughput. This drop can be counteracted by increased main ion throughput, however too much neon results in a back transition into the asymmetric divertor regimes suggesting a need for control of both main ion and impurity seeding levels to achieve a desired divertor state.

Keywords: SOLPS-ITER, SPARC, detachment, divertor, thermo-electric, hysteresis

(Some figures may appear in colour only in the online journal)

* Author to whom any correspondence should be addressed.

1. Introduction[3]

The SPARC tokamak is a compact ($R_0 = 1.85$ m) high-field ($B_0 = 12.2$ T) device with a primary goal of achieving scientific breakeven, $Q > 1$ [1, 2]. The compact size and high field strength of SPARC lead to extreme power exhaust and control challenges for the divertor. The heat flux width λ_q in the scrape-off-layer (SOL) is expected to be in the range of 0.18–0.43 mm [3] from experimental scaling relationships and theoretical models [4–6] (although simulations and experimental results indicate turbulence may broaden the power channel [7–10]). To avoid damage to the plasma facing components (PFCs) and unacceptable tungsten sputtering, several strategies are considered to either mitigate or reduce the deposited heat flux $q_\perp$ and electron temperature T_e at the divertor. These include strike point sweeping, extrinsic impurity seeding, and advanced divertor configurations such as the *x*-point target [3, 11]. SPARC can also operate in a double-null magnetic topology to share the power flux between the upper and lower divertors, significantly reducing power to the inner divertors.

The SPARC divertor was designed assuming conservative conditions; single-null operation with 29 MW of power crossing the separatrix P_{SOL} and a λ_q down to 0.14 mm [3]. Plasma boundary simulations using SOLPS-ITER [12] (hereafter abbreviated as SOLPS) and UEDGE [13] were used to inform the divertor design [3, 14] and requirements for the gas puff actuator and pumping systems [15]. Codes such as SOLPS have long been used in the process of divertor design [16] and to map out the expected operational regimes of future devices such as ITER [17].

Here we present an expanded numerical study using SOLPS of plasma conditions for the SPARC divertor and SOL, considering a range of assumed values for the cross-field transport coefficients in the SOL (which determine λ_q), two input power levels (10 and 29 MW, corresponding to 2/3-field and full-field operation [1]), different levels of neon impurity seeding, and several locations of the main ion fueling puff valve. A biased lower single null ($dR_{sep} = -2$ cm) topology is used, corresponding to the initial results presented in [3], however the PFC geometry has been updated. Both steady-state and time-dependent SOLPS simulations are employed, with the latter used to map out the operational phase space instead of to model plasma dynamics as studied in other work [18, 19].

The primary goal is to inform expected divertor conditions in pure deuterium plasmas, which have the maximum challenge from the divertor perspective, for a range of λ_q values. This information can be used to determine impurity seeding levels for the target divertor scenario. SPARC is a short pulse tokamak ($t_{flattop} < 10$ s) with inertially cooled tungsten divertor tiles. The maximum tolerable heat flux is thus a function of the pulse length and the strike point sweeping speed. For the purposes of this paper, a target of $\approx$30 MW m^{-2} is used, which enables a fairly wide operating space. For the 10 MW scenario, the effect of neon seeding on the divertor and upstream conditions are also explored. Strike point sweeping is not directly considered here, as fluid plasma boundary transport codes typically use a field-aligned computational mesh to overcome the strongly anisotropic transport and the magnetic topology cannot be varied in a given SOLPS simulation. Couplings to codes such as HEAT [20] are being developed, which can map the heat flux from SOLPS to the divertor as the strike point position changes. Transient heat loads caused by edge localized modes (ELMs), off-normal events, or 3D fields may be important for SPARC but are beyond the scope of this work.

The paper is organized as follows. In section 2 the SOLPS simulation setup is presented, including how the heat flux width depends on the input cross-field transport coefficients. Section 3 discusses the predicted divertor conditions for unseeded plasmas with 10 and 29 MW of P_{SOL} with the electron density at the outboard midplane $n_{e,sep}^{OMP} \approx 1 \times 10^{20}$ m^{-3}. Density scans, actuated by a core particle source for numerical stability, are used to identify a bifurcation in the divertor conditions where one divertor has significantly higher temperatures and parallel currents carry a large fraction of the parallel heat flux in the SOL. Above a threshold upstream density the divertors become more symmetric, and the parallel SOL current is small. The general behavior exists across a range of transport coefficients, fueling locations, and fixed fraction impurity concentrations. In section 4, neon seeding is introduced to 10 MW simulations with conservative λ_q assumptions to identify potential operational points with acceptable peak divertor energy fluxes, upstream density, and separatrix-averaged impurity concentrations. The inverse scaling of $n_{e,sep}^{OMP}$ with impurity content can cause a back-transition to the bifurcated divertor regime, however this can be counteracted by increased fuel ion throughput with no observed 'clamping' of the upstream density over the range explored.

2. Simulation setup

2.1. General SOLPS-ITER setup

Simulations are performed using version 3.0.8 of the SOLPS-ITER code [12, 21]. SOLPS solves a set of coupled fluid plasma equations (B2.5) with kinetic neutral transport and plasma-surface interactions handled by the EIRENE Monte Carlo code [22].

The computational mesh for the simulations presented here is shown in figure 1. The colored region consists of quadrilateral cells aligned with the magnetic field for plasma and neutral transport (quads subdivided into triangles), while the black region consists of triangular cells where only neutral transport is considered. The plasma mesh has a radial width of $\sim$4 mm in the SOL at the outboard midplane (OMP), limited by intersection of the SOL flux tubes with the PFC structure (while

[3] This manuscript has been authored in part by UT-Battelle, LLC, under Contract DE-AC05-00OR22725 with the US Department of Energy (DOE). The publisher acknowledges the US government license to provide public access under the DOE Public Access Plan (http://energy.gov/downloads/doe-public-access-plan.)

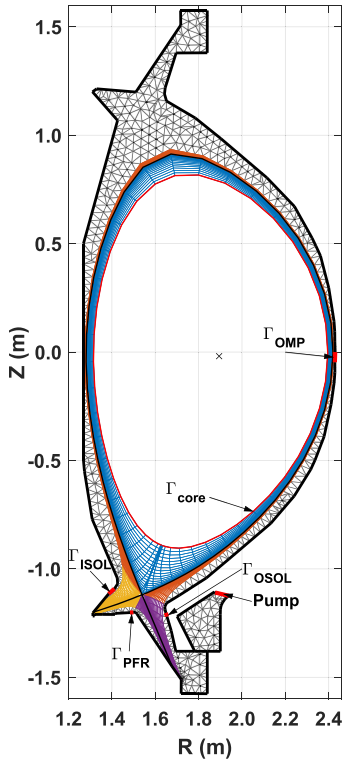

Figure 1. Computational mesh used for SOLPS-ITER simulations and SPARC V2y PFC geometry. Location of the pump surface and particle inputs are shown in red.

leaving a small volume to be triangulated for EIRENE). The PFC geometry corresponds to the version 'V2y' of the SPARC design, with tungsten used as the wall and divertor material, but not included as a plasma species in the simulation. A pumping volume was added approximating the (experimentally non-axisymmetric) subdivertor region, with the upper surface indicated set with a recycling coefficient $R = 0.95$ (surface area of 0.7758 m^2 corresponding to an effective pumping speed of $\sim$12 $m^3\,s^{-1}$). All other surfaces are treated as fully recycling, $R = 1$. Further details on the pumping assumptions and the effect of louver actuators (a set of angled slats used to control gas flow) is presented in [15]. The position of particle inputs used are also indicated in red in figure 1, with Γ_{core} corresponding to a D^+ source across the core boundary, and Γ_{OMP}, Γ_{OSOL}, Γ_{ISOL}, and Γ_{PFR} locations where D_2 or neon gas is injected. The core boundary condition is selected to return incident neutral particles as fully stripped ions, although for the SPARC conditions the neutral flux to this boundary is small. Drift-compatible boundary conditions are used, see discussion in [23].

2.2. Selection of cross-field transport coefficients

The fluid plasma transport in SOLPS is classical in the parallel direction (Braginskii [24] or Balescu [25]), with flux limiters used to prevent momentum and heat fluxes from exceeding the free streaming limit. A heat flux limiter coefficient (α following the definition in [26]) value of 0.15 is used here for electron heat transport, and 0.5 used for all other terms (ion heat, parallel momentum and thermo-electric and friction coefficients).

The cross-field transport is described by computed drift terms (deactivated for all results here) and an ad-hoc term representing turbulent transport set by user-defined diffusivities (and optionally, convective velocities, which are not used here). When performing interpretive simulations an effective radial profile of the cross-field diffusivities can be inferred to best match experimentally measured density and temperature profiles. Poloidal variation, following ballooning transport scaling [27–29] or scaling the transport in different regions [30] are sometimes used to improve the match to experimental data. When performing predictive simulations, on the other hand, the cross-field transport coefficients must be constrained by empirical or theoretical predictions. Coupling to a turbulent transport solver [31, 32] is generally too computationally expensive to be tractable, although recent work has incorporated a reduced k-epsilon turbulence model to SOLPS and SOLEDGE2D [33–35].

In the initial SPARC divertor scoping studies with SOLPS [3], a simple radial profile of the diffusivities was applied, with a constant value in the core to 1 mm inside the separatrix and another value applied in the far core and SOL. No poloidal variation in the coefficients is applied. The SOL particle diffusivity $D_\perp = 0.1\,m^2\,s^{-1}$, also used in UEDGE simulations [14], results in a radial density decay length of $\approx$10–20 mm. The SOL thermal diffusivity $\chi_\perp$ was then varied to approximately yield a heat flux decay length consistent with predictions from empirical scaling. It was found that $\chi_\perp = 0.01\,m^2\,s^{-1}$ gave λ_q of $\approx$0.14 mm, which was slightly smaller than the lower range in [3], leading to a conservative estimate for the divertor conditions. The core values of $\chi_\perp = 0.1\,m^2\,s^{-1}, D_\perp = 0.3\,m^2\,s^{-1}$ were not selected to match any predicted pedestal and core profiles [36–38]. The core transport is not the focus of this work, matching the pedestal and core profiles requires iterative coupling beyond the scope of this paper. Addition of a core transport barrier typically does not have a large effect on the SOL conditions (see e.g. [39]), but can affect core impurity content and neutral particle penetration, which will be important for future core-pedestal-SOL integration studies.

The narrow λ_q was considered a conservative starting point to inform the SPARC divertor design. To assess the impact of λ_q on the predicted operating space, the SOLPS simulations have been performed for a range of SOL cross-field diffusivities. The SOL $\chi_\perp$ and $D_\perp$ are scaled by a constant factor ranging from 1 to 16, referenced throughout this paper by the $\chi_\perp$ values. The core values are left unchanged. Figure 2 shows profiles of $q_{||}$ (comprising conduction and convection, including potential energy from ionization) evaluated at the poloidal position of the outer x-point and plotted against the distance from the separatrix at the OMP $(s - s_{sep})_{OMP}$ for a range of $\chi_\perp$.

For the cases shown, $P_{SOL} = 10$ MW and the ion particle flux through the core boundary is varied to achieve a relatively low upstream density ($n_{e,sep}^{OMP} \approx 1 - 3 \times 10^{19}\,m^{-3}$) where the

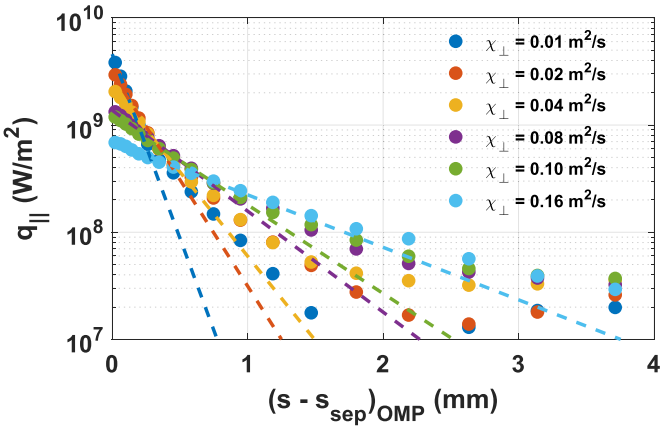

Figure 2. Parallel heat flux density, evaluated at the poloidal position of the outer X-point mapped to the outboard midplane for a range of cross-field SOL diffusivities. Dashed lines indicate exponential fits using values from near-SOL flux tubes where single exponential behavior is observed.

Table 1. Dependence of the heat flux width λ_q on the cross field diffusivity $\chi_\perp$ for near-SOL flux tubes under most attached conditions from figure 3.

$\chi_\perp$ (m^2 s^{-1})	0.01	0.02	0.04	0.08	0.10	0.16
λ_q (mm)	0.15	0.20	0.30	0.45	0.55	0.90

plasma is in an attached state (consistent with the experimental database used to develop the λ_q scaling [4]). The dashed lines in figure 2 are fits of the form $q_{||}(s-s_{\rm sep})_{\rm OMP} = q_{||0}\exp(-(s-s_{\rm sep})_{\rm OMP}/\lambda_{\rm q})$ using data from the near-SOL attached flux tubes. Table 1 lists the λ_q values for the cases shown in figure 2. It was found that the heat flux width is not a strong function of the input power, with $\chi_\perp$ of 0.01 m^2 s^{-1} resulting in λ_q of ≈0.15 mm, approximately the same value as found at 29MW [3].

Figure 3 shows fit values for λ_q as function of $\chi_\perp$ for several values of $n_{\rm e,sep}^{\rm OMP}$, indicated by the filled symbol color. A clear broadening of λ_q with increasing $n_{\rm e,sep}^{\rm OMP}$ at fixed $\chi_\perp$ is found. While some λ_q broadening with increasing density is expected as the parallel transport becomes flux limited and dissipation increases, an additional broadening is observed here due to flow reversal and redistribution of parallel current driven heat fluxes that extend through the SOL, as discussed in section 3.3. The dashed black line in figure 3 represents a linear fit to the data points at low density (figure 2), where both divertors are strongly attached. In this way the λ_q values at the lowest density (table 1) are representative of the challenge to achieve acceptable conditions at the outer divertor. Note that only cases with $\chi_\perp$ up to 0.1 m^2 s^{-1} are considered below, as the heat flux width approaches the radial grid width even at low density.

The effect of the ratio of $D_\perp/\chi_\perp$ has not yet been explored extensively for SPARC scenarios. This ratio was varied from 10 to 1/3 (the latter value is a commonly used ratio, including

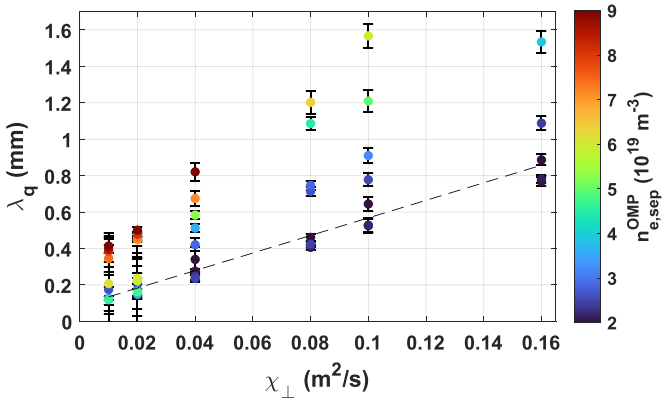

Figure 3. Fit values to the heat flux width for a range of cross-field diffusivities and separatrix electron densities at the OMP. Dashed black line is a linear fit to the low-density, attached divertor cases.

for most of the ITER database [17]) for $\chi_\perp = 0.02\,{\rm m}^2\,{\rm s}^{-1}$ at a constant core density boundary condition of 5×10^{19} m^{-3}. It was found that the fit value of λ_q only weakly changed from 0.17 to 0.20 mm for this range of $D_\perp/\chi_\perp$.

3. Divertor conditions for unseeded plasmas

3.1. Steady-state profiles at constant upstream density

Figure 4 shows upstream (OMP) profiles of electron temperature and density for a range of cross-field diffusivity values and two power levels, $P_{\rm SOL}$ = 10 MW and 29 MW. The corresponding radial profiles at the inner and outer divertor targets are shown in figures 5 and 6, respectively. The particle throughput was controlled through the core D$^+$ flux, with the level adjusted to give $n_{\rm e,sep}^{\rm OMP} \approx 1\times10^{20}$ m^{-3}, corresponding to the core scenarios described in [40]. The sensitivity of the results on the fueling location will be discussed in section 3.4. In general, a core particle source is found to be the most numerically stable, allowing for efficient scans of the upstream density to be performed. At full current the Greenwald density limit is ≈8.4×10^{20} m^{-3} [40], so the $P_{\rm SOL}$ = 10 MW scenarios are at $f_{\rm GW} \approx 0.25$, and $f_{\rm GW} \approx 0.35$ at full current ($P_{\rm SOL}$ = 29 MW), assuming a density profile such that $f_{\rm GW} = <n_{\rm e}>/n_{\rm GW} = 2n_{\rm e,sep}^{\rm OMP}/n_{\rm GW}$.

Table 2 lists the predicted inner and outer divertor plasma parameters $n_{\rm e}$, $T_{\rm e}$, $\Gamma_{\perp,{\rm i}}$, and $q_\perp^{\rm plasma}$ at the separatrix and the maximum value along the divertor for each $P_{\rm SOL}$ and $\chi_\perp$ value (the latter in parentheses). The total energy flux includes contributions from radiation $q_{\rm rad}$, neutral particles $q_{\rm neut}$, and plasma particles $q_{\rm plasma}$. The plasma heat flux $q_{\rm plasma}$ comprises conduction $q_{\rm cond} = n_{\rm e}\chi_{||{\rm e}}\nabla_{||}T_{\rm e} + n_{\rm i}\chi_{||{\rm i}}\nabla_{||}T_{\rm i}$, convection $q_{\rm conv} = \frac{5}{2}(\Gamma_{||{\rm e}}T_{\rm e} + \Sigma_{\rm a}\Gamma_{||a}T_{\rm a}) + \frac{1}{2}\Sigma_{\rm a}\Gamma_{\rm a}m_{\rm a}u_{\rm a}^2$, heat flux from the thermoelectric current $q_{{\rm therm}j} = -\alpha T_{\rm e}j_{||}/e$ and potential energy deposited on the target through recombination $q_{\rm pot} = \Sigma_{\rm a}\Gamma_{\rm a}\epsilon_{\rm a}^{\rm pot}$, minus the kinetic energy of reflected atoms and molecules originating from plasma ions. There can also be a heat flux caused by the electrostatic potential at the sheath

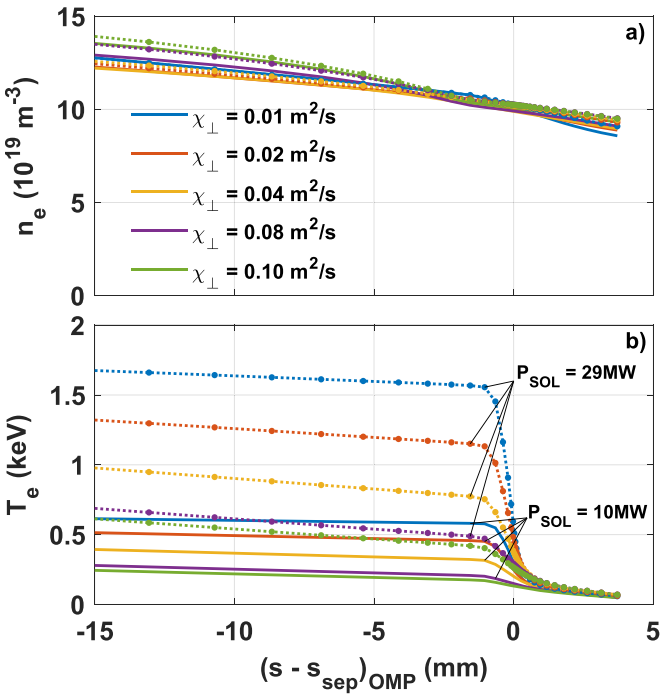

Figure 4. Upstream (OMP) profiles of electron density and temperature for a range of cross-field SOL diffusivities and two input power levels ($P_{\mathrm{SOL}} = 10$ MW solid lines, $P_{\mathrm{SOL}} = 29$ MW dashed lines), with the particle throughput selected to give $n_{\mathrm{e,sep}}^{\mathrm{OMP}} \approx 1 \times 10^{20} \mathrm{m}^{-3}$.

entrance if the targets are floating with a common device ground, see appendix B of [41]. Under the weakly dissipative (unseeded) conditions considered here, the power carried by the plasma is ≈95% of the total deposited power; loads from incident neutral particles and radiation are small (see section 4 for more detail). The fraction of the incident plasma power reflected as energetic neutral atoms can be relatively high (≈10%–40%), however, due to the high particle and energy reflection coefficients of tungsten.

The conditions at the outer target at low values of λ_q illustrate the challenge to achieve acceptable divertor conditions due to the compact size of SPARC. At low values of $\chi_\perp$ the peak n_e, T_e, $\Gamma_{\perp,\mathrm{i}}$ and $q_\perp^{\mathrm{plasma}}$ at $P_{\mathrm{SOL}} = 10$ MW are on the order of those predicted for ITER outer divertor at $P_{\mathrm{SOL}} = 100$ MW at low seeding levels [17, 39]. At higher $\chi_\perp$ and λ_q levels, the predicted conditions at $P_{\mathrm{SOL}} = 10$ MW are more manageable. At full power ($P_{\mathrm{SOL}} = 29$ MW) the peak $q_\perp$ and $T_{\mathrm{e,sep}}^{\mathrm{outer}}$ at the outer target are well beyond tolerable levels for the range of $\chi_\perp$ and λ_q considered, requiring mitigation in the form of impurity seeding or strike point sweeping to achieve long pulse lengths.

At $n_{\mathrm{e,sep}}^{\mathrm{OMP}} \approx 1 \times 10^{20}$ m^{-3}, the steady-state peak values of T_e and $q_\perp$ on the outer target significantly exceed those on the inner target. At low upstream densities, however, the situation is reversed, as will be shown next through a combination of steady-state and time-dependent simulations. To explore this topic in more detail, a combination of steady-state and time-dependent simulations are used.

3.2. Mapping operational space with time-dependent simulations

Time-dependent SOLPS-ITER simulations have been used for several purposes, including investigating dynamic plasma conditions [19, 42]; developing reduced models and control strategies [18]; simulating edge localized modes [43, 44]; and studying gas injection and pumping system dynamics [15, 45, 46]. In general, either the B2.5 or the EIRENE modules can be run dynamically, or both can be run in time-dependent modes to achieve fully time-dependent simulations. For more details see [15, 19].

Here we employ time dependent B2.5 simulations with EIRENE run in a quasi-steady-state (QSS, meaning all neutral trajectories are run until terminated by plasma-neutral interaction or absorption) manner, with slowly varying inputs used to effectively scan a wide range of steady-state scenarios. Figure 7 shows an example of such a simulation, using $\chi_\perp = 0.01$ m^2 s^{-1} and $P_{\mathrm{SOL}} = 10$ MW starting from a steady-state initial condition at low $n_{\mathrm{e,sep}}^{\mathrm{OMP}}$. The particle throughput is slowly ramped up and down (panel a), and the resulting change in separatrix electron density and temperature, and the integrated $\Gamma_{\perp,\mathrm{i}}$ and $q_\perp^{\mathrm{plasma}}$ at each target are shown. The throughput is controlled via Γ_{core}, which typically results in the best numerical stability of the code (larger time steps can be taken). Dependence of the results on fueling location is considered later.

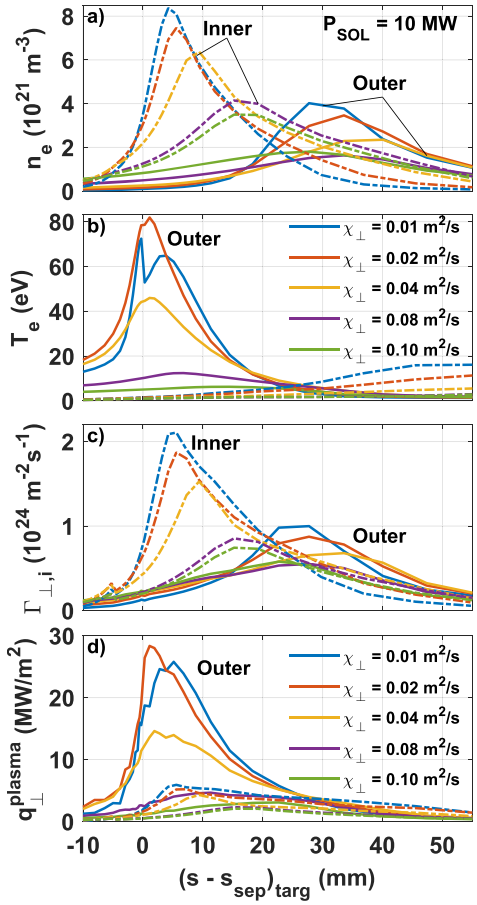

Figure 5. Radial profiles of (*a*) electron density, (*b*) electron temperature, (*c*) ion particle flux density, and (*d*) energy flux carried by the plasma at the inner (dashed line) and outer (solid line) targets for $P_{\mathrm{SOL}} = 10$ MW and a range of cross-field SOL diffusivities.

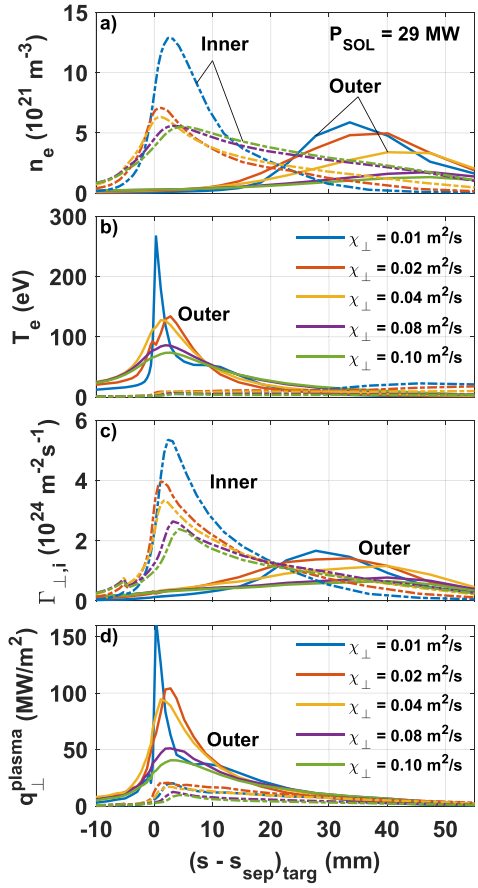

Figure 6. Radial profiles of (*a*) electron density, (*b*) electron temperature, (*c*) ion particle flux density, and (*d*) energy flux carried by the plasma at the inner (dashed line) and outer (solid line) targets for $P_{\mathrm{SOL}} = 29$ MW and a range of cross-field SOL diffusivities.

Initially, $P_{\mathrm{targ}} = \int q_{\perp} \mathrm{d}A$ and $T_{\mathrm{e,sep}}^{\mathrm{targ}}$ are similar at each target. There is then a period ($t < 0.5$ s) where the $P_{\mathrm{targ}}^{\mathrm{inner}} > P_{\mathrm{targ}}^{\mathrm{outer}}$ and $T_{\mathrm{e,sep}}^{\mathrm{outer}} > T_{\mathrm{e,sep}}^{\mathrm{inner}}$, followed by a sharp reversal of these conditions. The conditions return to the initial asymmetry at $t \approx 1.7$ s. The divertor state clearly exhibits hysteresis (asymmetric about $t = 0.9$ s). Note that the integrated particle flux to each divertor never shows rollover behavior, and $q_{\perp}^{\mathrm{plasma}}$ to the outer divertor only slightly reduces at the highest $n_{\mathrm{e,sep}}^{\mathrm{OMP}}$, indicating the divertor conditions are not reaching detachment and only weak power dissipation occurs in the outer divertor volume.

A subset of these data sets are shown in a phase space diagram in figure 8. Here the time-dependent runs are plotted as lines, and a set of steady-state simulations are shown as circular symbols. The arrows indicate the direction of increasing time, corresponding to figure 7. It can be seen that the time-dependent simulations generally agree well with the steady-state solutions, and can be used to efficiently map out large regions of the operating space. If the simulation outputs change rapidly in time, e.g. from $0.45 < t < 0.5$ s, the numerical settings can be adjusted to better resolve the dynamic behavior. In this range no steady-state solutions exist. For the data shown in orange and blue in figures 7 and 8, $\mathrm{d}t = 1 \times 10^{-4}$ with numerical relaxation factors set to 1.0. The dashed black lines in figure 8 show the solution with $\mathrm{d}t = 1 \times 10^{-5}$, where the sharp transition better resolved. In regions of solution space with strong non-linearity (e.g. low T_{e} where the plasma-neutral reactions change rapidly), relaxation factors <1.0 with fixed-point iteration may be necessary for code convergence.

The region with hysteresis is clearly observed in the phase space diagram. Here we identify three regions of operating space used to characterize the behavior, labeled in figure 8 and table 3.

In Regime 1, accessed from a low density initial state, the inner divertor has higher temperatures than the outer divertor and majority of the power goes to the inner target. Regime 1 is given the descriptive label 'Hot Inner Cold Outer' (HICO). In Regime 2 the situation is reversed, and is accessed from a high density initial state, referred to as 'Hot Outer Cold Inner (HOCI)'. The two regimes overlap for a range of $n_{\mathrm{e,sep}}^{\mathrm{OMP}}$ and particle throughput. As will be shown in section 3.3, Regimes 1 and 2 are characterized by a significant fraction of the parallel heat flux coming from parallel currents driven

Table 2. Divertor conditions for two power levels for a range of cross-field SOL diffusivities. The first number in each column gives the value at the separatrix and the second number in parentheses is the maximum value along the divertor plate in the SOL.

	10 MW				
$\chi_\perp$ ($m^2\,s^{-1}$)	0.01	0.02	0.04	0.08	0.10
T_e^{outer} (eV)	62.6 (64.8)	78.5 (81.8)	44.4 (45.9)	10.2 (12.4)	4.9 (6.3)
T_e^{inner} (eV)	1.5 (16.1)	1.4 (11.6)	1.2 (6.9)	0.9 (3.1)	1.0 (2.9)
n_e^{outer} ($10^{21}m^{-3}$)	0.1 (4.0)	0.2 (3.5)	0.2 (2.3)	0.5 (1.6)	0.8 (1.8)
n_e^{inner} ($10^{21}m^{-3}$)	3.5 (8.4)	3.1 (7.5)	2.2 (6.4)	1.3 (4.1)	1.1 (3.5)
$q_\perp^{outer}$ (MWm^{-2})	22.2 (30.5)	27.7 (33.3)	15.0 (17.6)	3.6 (6.7)	1.8 (4.6)
$q_\perp^{inner}$ (MWm^{-2})	2.6 (8.1)	2.1 (7.1)	1.3 (5.6)	0.6 (3.0)	0.6 (2.7)
$\Gamma_\perp^{outer}$ ($10^{24}m^2\,s^{-1}$)	0.1 (1.0)	0.2 (0.9)	0.2 (0.7)	0.2 (0.6)	0.2 (0.6)
$\Gamma_\perp^{inner}$ ($10^{24}m^2\,s^{-1}$)	0.8 (2.1)	0.7 (1.9)	0.4 (1.5)	0.2 (0.9)	0.2 (0.7)
	29 MW				
$\chi_\perp$ ($m^2\,s^{-1}$)	0.01	0.02	0.04	0.08	0.10
T_e^{outer} (eV)	177.1 (266.7)	89.6 (134.0)	114.0 (127.6)	78.2 (86.0)	66.7 (73.7)
T_e^{inner} (eV)	2.3 (22.7)	6.3 (18.0)	4.2 (12.8)	2.2 (6.5)	2.0 (5.6)
n_e^{outer} ($10^{21}m^{-3}$)	0.1 (5.9)	0.2 (5.0)	0.2 (3.4)	0.3 (1.7)	0.3 (1.3)
n_e^{inner} ($10^{21}m^{-3}$)	8.3 (12.9)	6.8 (7.1)	6.1 (6.3)	4.5 (5.6)	3.9 (5.5)
$q_\perp^{outer}$ (MWm^{-2})	121.4 (185.2)	71.8 (116.2)	83.5 (104.9)	46.0 (59.0)	35.4 (46.9)
$q_\perp^{inner}$ (MWm^{-2})	8.6 (32.8)	21.7 (36.5)	11.9 (29.4)	4.8 (19.8)	3.6 (16.1)
$\Gamma_\perp^{outer}$ ($10^{24}m^2\,s^{-1}$)	0.1 (1.7)	0.3 (1.4)	0.3 (1.2)	0.3 (0.8)	0.3 (0.7)
$\Gamma_\perp^{inner}$ ($10^{24}m^2\,s^{-1}$)	2.3 (5.4)	3.1 (4.0)	2.3 (3.3)	1.2 (2.6)	1.0 (2.4)

by temperature asymmetry between the targets. Regime 3 'Conventional' is more qualitative, starting where $T_{e,sep}^{outer}$ and P_{target}^{outer} begin to decrease with $n_{e,sep}^{OMP}$. In this regime $T_{e,sep}^{inner}$ is low while the outer divertor transitions through the high recycling regime (HRR) and eventually both divertors show low temperature and pressure loss at the highest densities. Significant dissipation only occurs for the highest $n_{e,sep}^{OMP}$ steady-state cases, beyond the time-dependent series. These high-density unseeded scenarios may not be operationally accessible, however, as f_{GW} is large (up to 1.2). The Conventional Regime does not exhibit any significant hysteresis.

The same general behavior exists in the phase space diagram for other $\chi_\perp$ values, as shown in figure 9 for $P_{SOL} = 10$ MW and the same gas throughput as in figure 7*(a)*. Here $T_{e,sep}^{outer}$ and $T_{e,sep}^{inner}$ are plotted in separate panels for clarity. In all cases a region of hysteresis exists, with the divertor conditions depending on whether the solution is approached from a high or low density state. The width of the overlap of the HICO and HOCI Regimes is reduced as $\chi_\perp$ increases. This is due to the smaller asymmetry in the divertor T_e profiles as $\chi_\perp$ is increased, namely that extremely large values of T_e do not occur for larger values of λ_q (see section 3.3 and figures 5 and 6). Figure 9 also shows how low temperature divertor conditions can be accessed at lower values of $n_{e,sep}^{OMP}$ as $\chi_\perp$ increases.

3.3. Hysteresis and parallel current driven heat flux

As discussed in previous sections, the inner and outer divertor conditions exhibit a region of hysteresis with sharp transitions depending on whether the solution is approached from a high or low density initial state. The width of the hysteresis region is reduced as $\chi_\perp$ is increased, but exists in each case. In this section, solutions with $\chi_\perp = 0.01$ $m^2\,s^{-1}$ are examined to determine the cause. While the desired steady-state SPARC operational scenarios may be in the Conventional Regime, at a higher $n_{e,sep}^{OMP}$ than where the hysteresis occurs, the HICO and HOCI Regimes are important to understand and may affect access to the steady-state density and require modified control strategies for fueling and impurity seeding.

Starting from a low density state both the inner and outer divertor are in strongly attached conditions, with high T_e and low n_e, as shown in figure 7. The deposited heat flux on the inner divertor, and therefore the divertor T_e required to exhaust this heat under sheath-limited conditions ($q \propto T_e^{3/2} n_e$) is larger on the inner divertor. This occurs because of the smaller wetted area ($\propto 2\pi R$) and the slightly higher magnetic field angle of incidence with the equilibrium used (≈0.75 vs 1.2 degrees at the outer and inner strike points, respectively). Note that these are the values used by SOLPS with an axisymmetric assumption and simplified PFC geometry, not the as-constructed values.

As the density is increased from this state, the outer divertor T_e drops more rapidly than at the inner divertor. As this in/out asymmetry in T_e increases, a parallel current arises, carrying power from the cold to the hot divertor via convection and further increasing the asymmetry. For a two-species deuterium plasma with $n = n_e = n_i$, the total classical parallel heat flux in the SOL is [24]

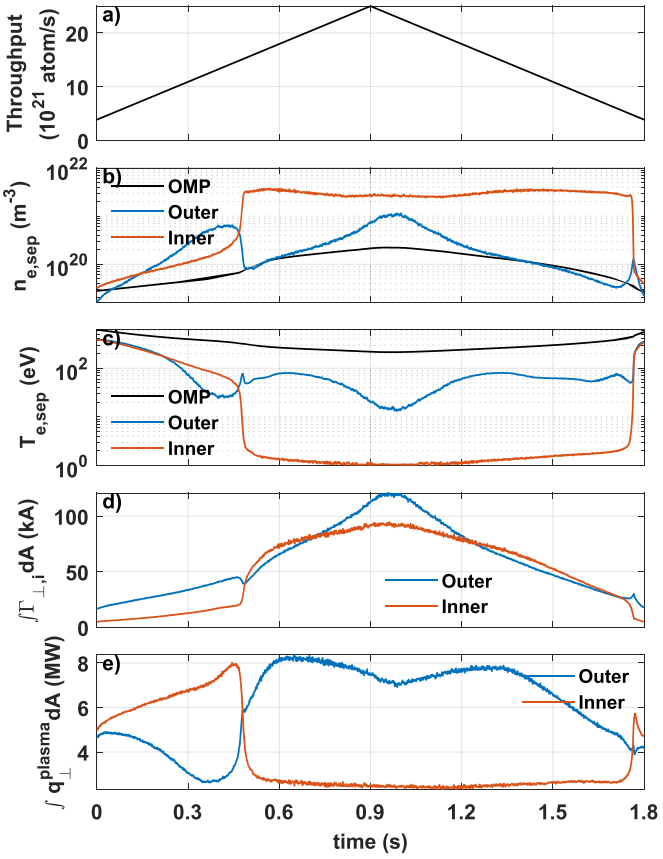

Figure 7. *(a)* Time-varying core ion flux input using $\chi_\perp = 0.01$ $m^2 s^{-1}$ and $P_{SOL} = 10$MW and the response in (*b*) separatrix electron density at the OMP and each divertor, (*c*) separatrix electron temperature at the OMP and each divertor, (*d*) integrated ion flux to each divertor, and (*e*) power carried by the plasma to each divertor.

$$
\begin{aligned}
q_{||} &= q_{\text{cond}} + q_{\text{conv}} + q_{\text{therm}j} \\
&= -n\left(\chi_{||\text{e}}\nabla_{||}T_\text{e} + \chi_{||\text{i}}\nabla_{||}T_\text{i}\right) \\
&\quad + \left[\frac{5}{2}T_\text{i} + \frac{1}{2}mu^2\right]\Gamma_{||\text{i}} + \frac{5}{2}T_\text{e}\Gamma_{||\text{e}} - \alpha T_\text{e}\frac{j_{||}}{e} \qquad (1) \\
&= -n\left(\chi_{||\text{e}}\nabla_{||}T_\text{e} + \chi_{||\text{i}}\nabla_{||}T_\text{i}\right) \\
&\quad + \left[\frac{5}{2}\left(T_\text{e} + T_\text{i}\right) + \frac{1}{2}mu^2\right]\Gamma_{||\text{i}} - \left(\frac{5}{2} + \alpha\right)T_\text{e}\frac{j_{||}}{e},
\end{aligned}
$$

where $j_{||}/en = u_{||\text{i}} - u_{||\text{e}}$. From the parallel Ohm's law, $j_{||}/\sigma_{||} = -\nabla_{||}\Phi - (\alpha/e)\nabla_{||}T_\text{e} + (1/ne)\nabla_{||}p_\text{e}$ is driven by gradients in electron pressure, temperature, and electrostatic potential. In the last form of equation (1), the terms have been sorted into parallel conduction, those proportional to the ion parallel velocity $u_{||} = \Gamma_{||\text{i}}/n$, and those proportional to $j_{||}$. The contribution from the thermoelectric coefficient α is due to velocity dependence of the collision frequency [47]. For a deuterium plasma, $\alpha = 0.71$, and the heat flux proportional to $j_{||}$ is $q_{j_{||}} \approx -3.21 j_{||}T_\text{e}/e$.

The thermoelectric current and current-driven heat flux effects are captured by SOLPS [23, 48–50]. When there is temperature asymmetry between divertor plates connected by a flux tube, the result is a current-driven heat flux flowing from the colder to the hotter divertor. This results in a thermodynamic instability (positive feedback loop) that further increases the asymmetry, limited by instability [51] or when the other terms in equation (1) and the energy equation (e.g. cross-field transport and radiation) adjust to provide balance [52]. Divertor currents driven by the thermoelectric effect have been measured in experiments [53–55], described in 1D theoretical models [56, 57], and proposed as a mechanism for potential divertor flux control via biasing [50, 58]. From the SOLPS simulations it is difficult to separate the cause and effect of divertor temperature asymmetry and the parallel current that increases the asymmetry. The initial seed for the feedback effect may be due to the lack of symmetry in the PFC structure, or caused by variation in the radiated power leading to a bifurcation [56, 59]. Note that cross-field drift terms are

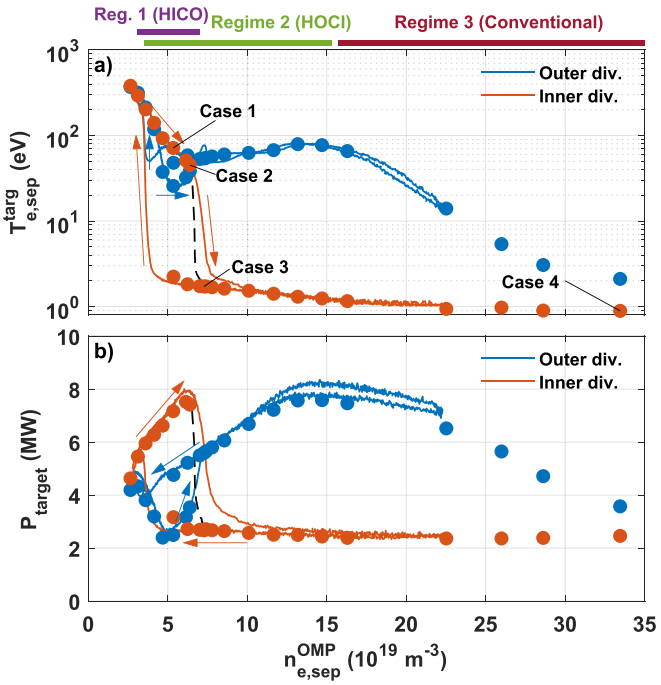

Figure 8. Phase space diagram of (*a*) divertor electron separatrix temperature and (*b*) total power carried by the plasma to each divertor. Lines are from the time-series data shown in figure 7 with arrows indicating the direction of time, symbols are from steady-state simulations. The dashed black line is from a time-dependent simulation with a smaller time-step to better resolve the sharp change between HICO and HOCI solutions.

Table 3. Description of the different divertor state 'Regimes' described in this paper.

Regime	Descriptive label	T_e asymmetry	$q_{||}$ asymmetry	SOL $j_{||}$
1	Hot inner cold outer (HICO)	$T_\text{e}^\text{inner} >> T_\text{e}^\text{outer}$	$q_{||}^\text{inner} >> q_{||}^\text{outer}$	Towards inner
2	Hot outer cold inner (HOCI)	$T_\text{e}^\text{outer} >> T_\text{e}^\text{inner}$	$q_{||}^\text{outer} >> q_{||}^\text{inner}$	Towards outer
3	Conventional	$T_\text{e}^\text{outer} > T_\text{e}^\text{inner}$	$q_{||}^\text{inner} \approx q_{||}^\text{outer}$	Small

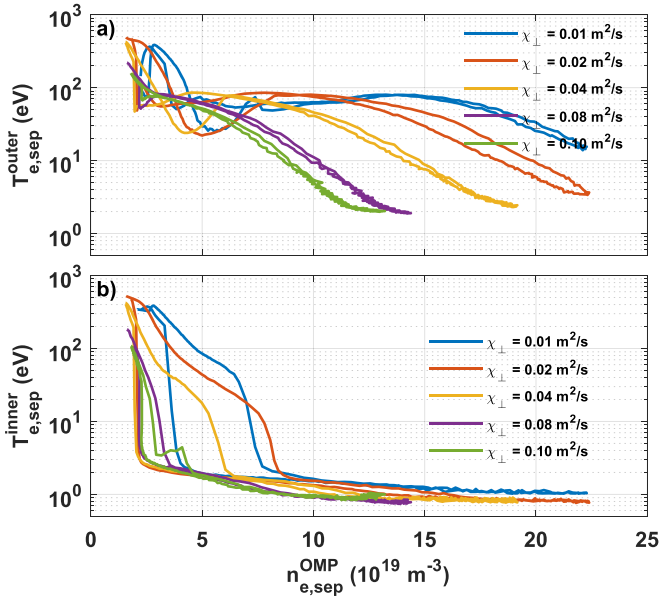

Figure 9. Phase space diagrams of (*a*) outer and (*b*) inner separatrix electron temperature versus $n^{\mathrm{OMP}}_{\mathrm{e,sep}}$ for several values of $\chi_\perp$.

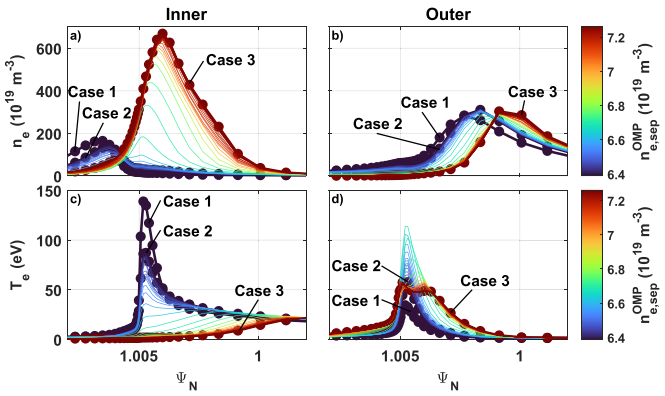

Figure 10. Profiles of n_e and T_e at the inner and outer divertor from just before to just after the transition, approached from a low density state. Line color indicates upstream density $n^{\mathrm{OMP}}_{\mathrm{e,sep}}$. Steady-state solutions are shown with symbols (pre-transition cases 1–2 and post-transition case 3). Time-dependent solutions are shown as lines without symbols.

not required to capture this effect in SOLPS, but their inclusion may modify the SOL current distribution [49, 50]. Hysteresis in the level of detachment has also been observed in simulations of devices such as ARC [60] and DTT [61].

Here we investigate solutions before and after the transition from a hot inner divertor (HICO) to a hot outer divertor (HOCI), starting from a low density solution. A similar bifurcation happens in the opposite direction during the transition from HOCI to HICO. Figure 10 shows steady-state electron temperature and density profiles (lines with symbols) at each divertor for two states before the transition, and one state after. These correspond to the cases numbered 1–3 in figure 8. The thinner lines in figure 10 are from a time-dependent simulation (dashed black line in figure 8) that attempts to resolve the dynamics of the bifurcation. Note that no stable steady-state solutions are possible in this range of the time-dependent simulation.

It can be seen that at $n^{\mathrm{OMP}}_{\mathrm{e,sep}} = 8.4\times10^{19}$ m^{-3} (case 1), T_e is larger at the inner divertor across the target (HICO). The n_e profile is correspondingly lower at the inner target. There is an increase in n_e in the inner target private flux region due to the change in PFC geometry angle in this region, leading to a $\approx$2$\times$ increase in the angle of incidence and also affects the direction of the reflected neutrals, increasing the local density. The solution just before the transition (case 2) has lower peak T_e on each divertor, and the ΔT_e is reduced for the first flux tubes in the SOL. During the transition between case 2 and case 3 the inner divertor T_e rapidly drops while n_e rises, while the opposite trend occurs at the outer divertor. High T_e values up to $\approx$100 eV near the outer separatrix are observed transiently before reaching the steady-state solution (case 3) where the T_e profile is broader with a double-peak like structure. On this side of the hysteresis region, the outer divertor is hotter than the inner divertor in the near-SOL (HOCI).

The total $q_{||}$, the $q^{\mathrm{cond}}_{||}$ and $q^{\mathrm{conv}}_{||} + q^{\mathrm{therm}j}_{||}$ components, as well as $u_{||\mathrm{i}}$ and n_e for each case is shown column-wise in figure 11. An additional high density solution (case 4), well into the Conventional Regime, is included for comparison. The poloidal distribution of the heat flux and ion flow in the first flux tube in the SOL is shown in figure 12 for each case. In these figures negative values are directed towards the outer target (red color in figure 11) while positive values are directed towards the inner target (blue color).

The conducted heat flux is directed towards the local target in each case (figures 11(*e*)–(*h*), and dashed orange line in figure 12). The convected + thermoelectric heat flux (figures 11(*i*)–(*l*) and green dot-dashed line in figure 12), on the other hand, changes sign depending on the divertor temperature asymmetry and the magnitude of $q_{j||}$ driven heat fluxes. In Case 1 (strongly HICO), $q^{\mathrm{conv}}_{||}$ is directed towards the inner divertor throughout the SOL. On the low field side (LFS), $q^{\mathrm{conv}}_{||}$ is directed against $q^{\mathrm{cond}}_{||}$, and the resulting $q^{\mathrm{tot}}_{||}$ is reduced in magnitude and radial width. That $q^{\mathrm{conv}}_{||}$ is dominantly driven by $j_{||}$ can be seen by comparing the 1D profile to $-3.21 j_{||} T_\mathrm{e}/e$ (purple line with symbols in figure 12) and the different structure as compared to the ion flow (figures 11(*m*)–(*p*) and black line in figure 12). The $u_{||\mathrm{i}}$ pattern is largely source-driven (compare n_e, figures 11(*q*)–(*t*). A region of flow reversal can be observed in the LFS SOL, which has strong SOL recycling flux, while the flow in the private flux region (PFR) has a stagnation point near the HFS, where the inner n_e (and Γ_i) profile peaks.

In case 2 (weakly HICO) the in/out T_e asymmetry is reduced, and correspondingly the magnitude of $q^{\mathrm{conv+therm}j}_{||}$ towards the inner divertor is smaller. In the first flux tube, as shown in figure 12, the total $q_{||}$ is mostly due to conduction. The $j_{||}$ driven heat flux is still the dominant contribution to $q^{\mathrm{conv+therm}j}_{||}$. A small region of flow reversal is observed in the inner SOL as the n_e and SOL recycling source increases.

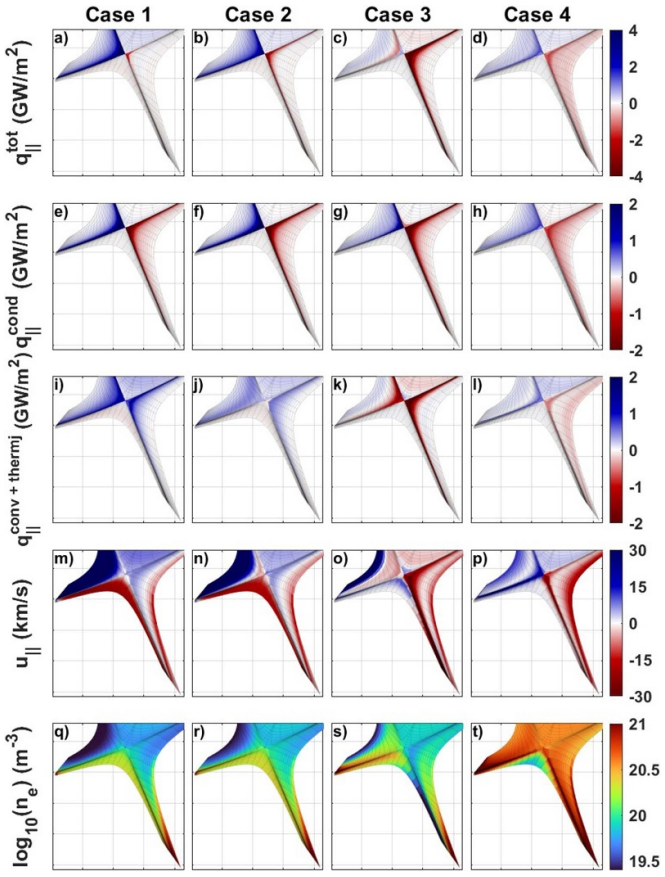

Figure 11. 2D profiles of (*a*)–(*d*) conducted heat flux, (*e*)–(*h*) convected heat flux, (*i*)–(*l*) parallel ion flow, and (*m*)–(*p*) electron density. The four columns correspond to the steady-state solutions as labeled in figure 8. Negative values are directed towards the outer target while positive values are directed towards the inner target.

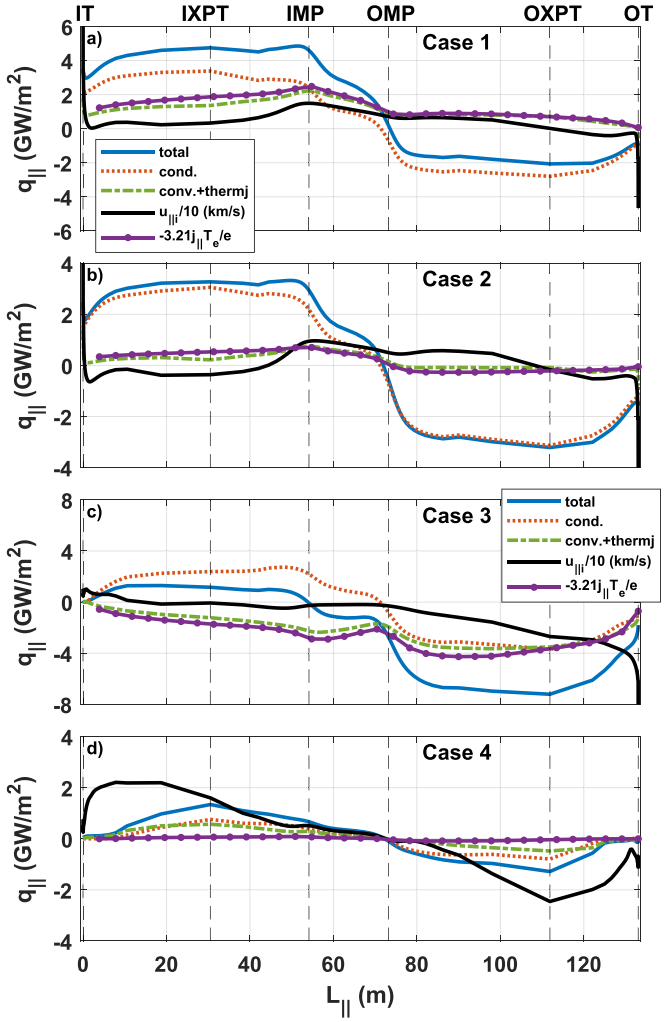

Figure 12. 1D poloidal profiles of total parallel heat flux $q_{||}$, components from conduction $q_{||}^{\mathrm{cond}}$ and convection + thermoelectric $q_{||}^{\mathrm{conv+therm}j}$ components, parallel ion flow $u_{||\mathrm{i}}$, and approximation to the $q_{||}$ carried by $j_{||}$. The profiles are for the first flux tube in the SOL, for four cases as labeled in figure 8 and corresponding to the columns in figure 11.

The broadening of the SOL power channel on the LFS can be observed in figure 11(*b*).

In case 3, following the transition to HOCI, the temperature asymmetry is reversed and $q_{||}^{\mathrm{conv+therm}j}$ is directed towards the outer target. Again $q_{||}^{\mathrm{conv}}$ is well approximated by $-3.21 j_{||} T_{\mathrm{e}}/e$, and competes or even surpasses $q_{||}^{\mathrm{cond}}$ on the HFS. The power channel on the LFS is now significantly wider, resulting in the broader T_{e} profile at the outer target as seen in figure 10. The $u_{||\mathrm{i}}$ pattern in the PFR is more symmetric as the HFS recycling in the PFR is reduced, and now dominated by the SOL source with flow reversal observed in the HFS SOL.

For contrast with the conditions around the hysteresis range, case 4 in the Conventional Regime shows a steady-state solution at $n_{\mathrm{e,sep}}^{\mathrm{OMP}} = 3.3 \times 10^{20}$ m^{-3}. Here the heat fluxes and $u_{||}$ patterns have a more 'typical' symmetric pattern, with a flow stagnation point near the OMP. The total $q_{||}$ in the near-SOL has roughly equal contributions from convection and conduction, and the $j_{||}$ driven heat flux is very small, meaning $q_{||}^{\mathrm{conv+therm}j} \propto u_{||\mathrm{i}}$.

A similar behavior is found for the other values of $\chi_{\perp}$, although the increased λ_q results in lower divertor T_{e} and reduced temperature asymmetry between the divertors. As such, the hysteresis region occurs at lower $n_{\mathrm{e,sep}}^{\mathrm{OMP}}$ as shown in figure 9.

The effect of impurity radiation on the hysteresis behavior was investigated using a fixed-fraction (f_z) impurity model available in SOLPS. The default model has a cooling curve $L_Z(T_{\mathrm{e}}) = f_z \cdot 2 \cdot 10^{-32}/(\hat{T}_{\mathrm{e}}^{\,3/2} + \hat{T}_{\mathrm{e}}^{\,-3})$, where $\hat{T}_{\mathrm{e}} = T_{\mathrm{e}}/T_{\mathrm{norm}}$ and $T_{\mathrm{norm}} = 15$ eV [62]. This function peaks T_{norm} and roughly approximates the cooling curve for nitrogen. The divertor temperature phase space is shown in figure 13 for several values of f_Z. The general trend is that, beyond the hysteresis range, lower divertor T_{e} can be reached at lower $n_{\mathrm{e,sep}}^{\mathrm{OMP}}$ as f_Z increases, as expected. The hysteresis and $j_{||}$ driven heat

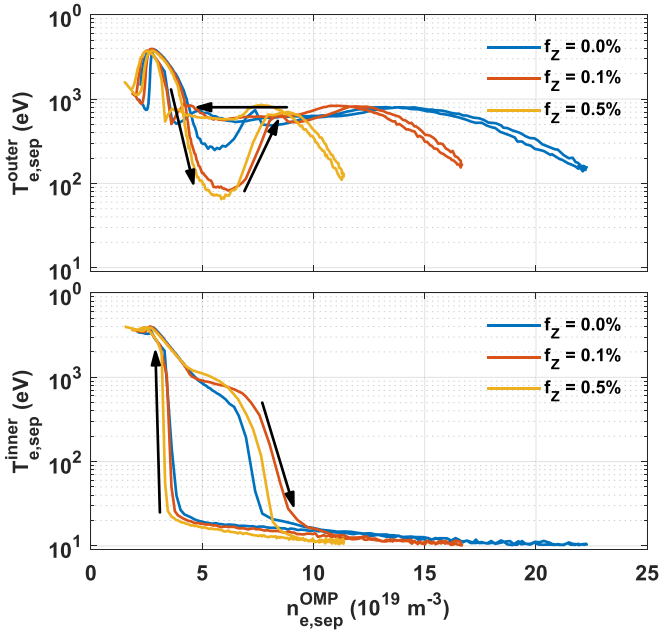

Figure 13. Outer and inner divertor separatrix electron temperature versus $n^{OMP}_{e,sep}$ for $f_Z = 0\%$ (blue), 0.1 % (red/orange) and 0.5% (yellow). All cases use $\chi_\perp = 0.01$ m^2 s^{-1} and $P_{SOL} = 10$ MW. Arrows indicate direction of time in gas throughput scan.

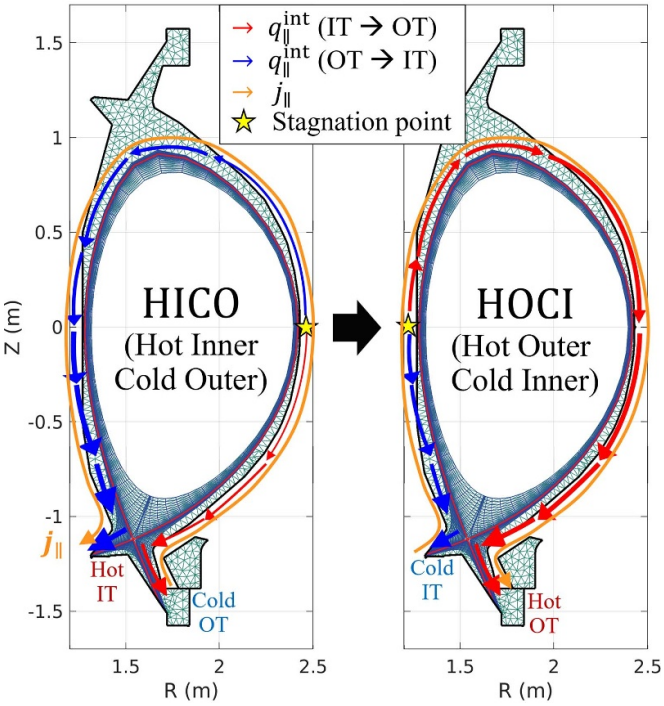

Figure 14. Schematic illustration of the parallel current and net parallel heat flux in the HICO (left) and HOCI (right) regimes.

flux actually somewhat increases in magnitude. This occurs because the L_Z curve is larger in the T_e range of the outer divertor, causing more effective cooling there, and increasing the parallel T_e gradient. At sufficiently high f_Z, even the low $n^{OMP}_{e,sep}$ cases would have reduced T_e on both divertors. These cases were not explored here, and results of including a higher fidelity impurity transport model are shown in section 4.

Figure 14 schematically illustrates the differences between the HICO and HOCI regimes. The orange arrow indicates the direction of $j_{||}$, while the red and blue arrows qualitatively show the direction and magnitude (line thickness) of the total $q_{||}$ in the near-SOL flux tubes. In the HICO regime, the parallel current flows from the cold outer target to the hot inner target, with the net $q_{||}$ profile having a stagnation point near the OMP. In the HOCI regime $j_{||}$ is reversed, flowing from the cold inner target to the hot outer target, and the $q_{||}$ stagnation point is near the inboard midplane (IMP). As the effective connection length for the power channel to the outer target is larger in the HOCI regime, there is an effective broadening in the heat flux width measured at the outer x-point, contributing to the effect seen in figure 3.

3.4. Effect of fueling location

The effect of the fueling location on the divertor solution was explored by varying the particle throughput from D_2 gas sources in EIRENE as labeled in figure 1, in addition to the D_+ source from the core shown in the previous sections. Here we focus on only two issues: whether the hysteresis behavior is specific to core fueling and a preliminary investigation into the relative fueling efficiency of each source location. Details of the effect of the puff location on the boundary plasma, including the effect on SOL impurity concentration will be presented in future work. A comparison of puff and louver actuators on particle control for SPARC are given in [15].

Figure 15 shows the divertor T_e phase space for time-dependent scans of the particle throughput for each source location. For the various puff locations the core D^+ source is held constant at 1.5e21 atoms s^{-1}, the minimum level used in the time-dependent scans presented above. It can be seen that the general hysteresis behavior is present for each case. Also, at sufficiently high density ($n^{OMP}_{e,sep} > 1.5 \times 10^{20}$) the divertor T_e is not strongly dependent on the particle source. (The ion flow pattern and friction force on impurity species could be affected, however [63].) The OMP puff location results in slightly higher divertor temperatures in the Conventional Regime than the other source locations, while the PFR puff results in the greatest level of divertor temperature asymmetry.

It was found that the numerical stability of the SOLPS simulation, and therefore the required timestep and EIRENE source nonlinearity relaxation settings, was dependent on the source location. In general, the core source was the most stable, while the ISOL, OSOL and PFR puff locations were the most unstable. This instability near regions of rapid change can be observed in the 'noisy' data for these locations in figure 15. The details of the bifurcation transition for each puff location has not been explored in detail, but the general trend is that source locations that preferentially increase n_e and decrease

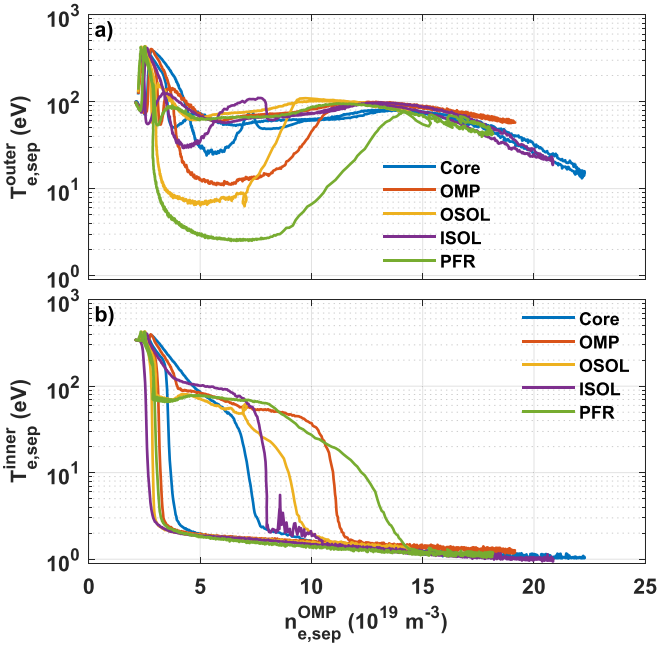

Figure 15. Outer and inner divertor separatrix temperature versus $n^{OMP}_{e,sep}$ for different particle source locations as labeled in figure 1.

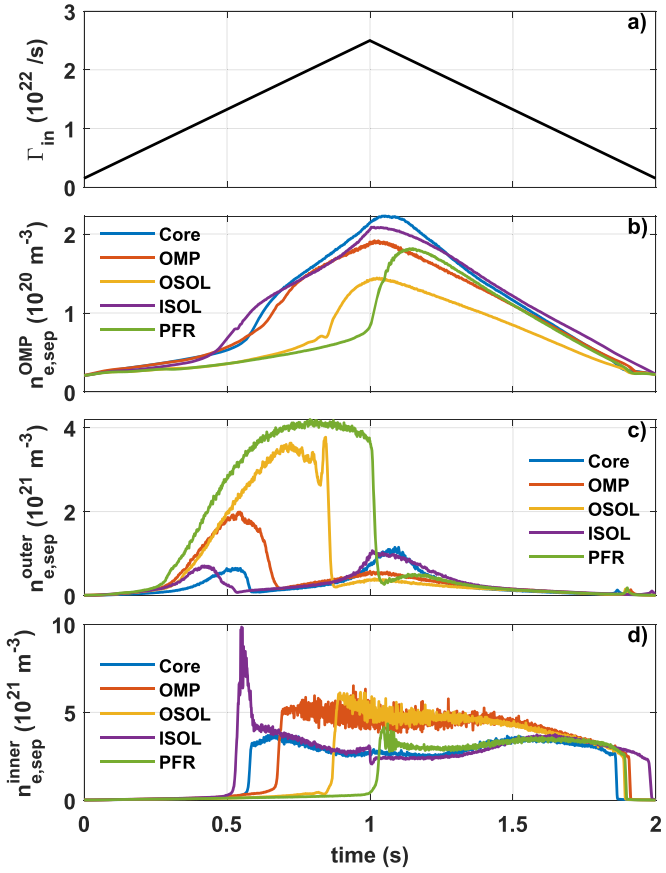

Figure 16. *(a)* Particle throughput and corresponding electron separatrix density at the (*b*) OMP, (*c*) outer divertor, and (*d*) inner divertor for several particle source locations as labeled in figure 1.

T_e at the outer divertor increase the initial temperature asymmetry (starting from a low $n^{OMP}_{e,sep}$ case) and therefore exacerbate the bifurcation. This includes the PFR puff, because the initial state has a higher PFR density (and near-SOL T_e) resulting in an increased neutral ionization mean free path.

The relative fueling efficiency, the ability of a source location to increase n_e in different regions for a given particle throughput, is shown in figure 16. In each case the total particle throughput is the same as a function of time (figure 16(*a*)), while $n_{e,sep}$ at the OMP, outer and inner divertor is shown in panels (*b*)–(*d*). The core, OMP, and ISOL puff locations result in a similar increase in $n^{OMP}_{e,sep}$, while the PFR and OSOL are less effective. The OSOL and ISOL puff are effective at increasing the local divertor density, while the PFR puff preferentially fuels the outer divertor when starting from a low density state for the reason described above. The relative fueling efficiency affects the threshold Γ_{D2} at which the HICO to HOCI transition occurs, with the OMP, ISOL, and Core cases bifurcating at a lower throughput level than the PFR and OSOL puff cases. After the HICO to HOCI bifurcation, and towards the maximum throughput where the divertor conditions are less asymmetric (Conventional Regime in figure 8), the differences between the puff locations are less dramatic. The transition from HICO to HOCI shows a puff-location dependence on the outer divertor, but the inner divertor response is more uniform and less sensitive to the puff location. No clear saturation of the upstream density with respect to the gas throughput is observed over the range explored. This effect is more clearly presented with steady-state simulations, as shown in the next section.

4. Simulations with impurity seeding

At high P_{SOL} impurity seeding is likely to be required even to reach the targeted levels (≈30 MW m^{-2}) to be exhausted using strike-point sweeping. Tungsten sputtering due to the high T_e will only exacerbate the challenge.

The effect of extrinsic impurity seeding is explored in SOLPS by injecting neon from the OMP (nitrogen is to be avoided due to tritiated ammonia production). Five series of steady-state SOLPS simulations with increasing levels of neon throughput Γ_{Ne} were performed starting from steady-state solutions with different levels of D_2 fueling from the OMP and $P_{SOL} = 10$ MW. The neon throughput was varied to reach a desired level of upstream separatrix neon concentration $\langle c_{Ne} \rangle = \sum n_{Ne}/n_e$ (sum over neon charge state) from 0% to 2%. The results are summarized in figure 17, with the symbols indicating the steady-state solutions (color corresponding to concentration). The solid grey trace is from a time-dependent simulation with no seeding, $\Gamma_{Ne} = 0$. Two initial states are from the HICO and HOCI Regimes at the same level of D_2 throughput, $\Gamma_{D2} = 1 \times 10^{22}$ atoms s^{-1}. The other three initial states, $\Gamma_{D2} = 2 \times 10^{22}, 2.5 \times 10^{22}$, and 3×10^{22} atoms s^{-1} are started in Conventional Regime.

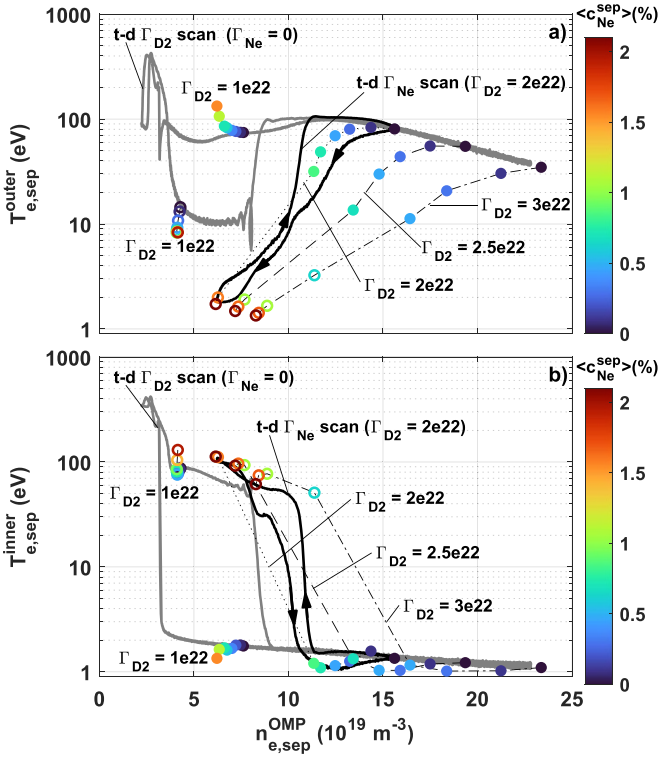

Figure 17. Dependence of (*a*) outer and (*b*) inner divertor separatrix T_e on upstream density and main ion and neon gas throughput with $P_{SOL} = 10$ MW. The light grey curve indicates a time-dependent Γ_{D2} scan with $\Gamma_{Ne} = 0$. From five initial conditions with fixed Γ_{D2}, Γ_{Ne} was scanned to result in steady state solutions with a desired $\langle c_{Ne} \rangle$ level (symbols, with $\langle c_{Ne} \rangle$ per color bar). Open symbols indicate a back transition to the HICO regime. Solid black curve shows a time-dependent Γ_{Ne} simulation for comparison to the steady-state solution. Arrows indicate direction of time in seeding scan.

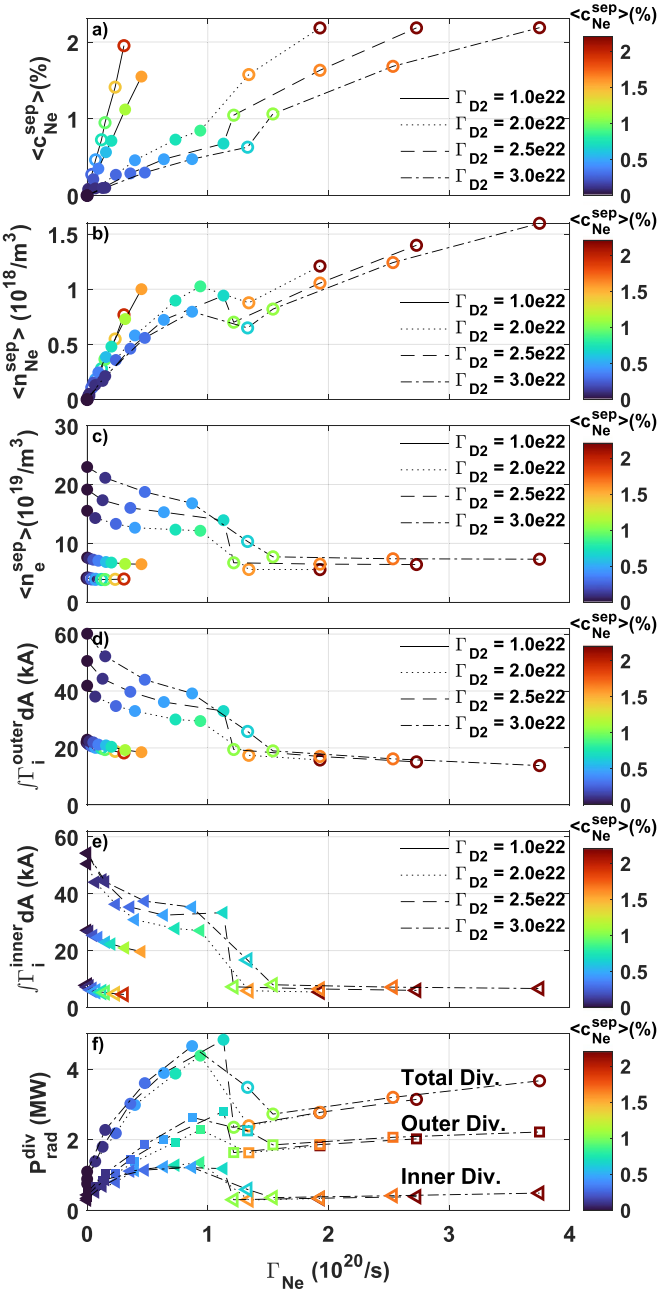

Figure 18. Dependence of separatrix averaged (*a*) neon concentration, (*b*) neon density, (*c*) electron density, integrated ion flux to the (*d*) outer and (*e*) inner divertor, and (*f*) radiated power from the inner and outer divertor volumes with $P_{SOL} = 10$ MW. Color indicates $\langle c_{Ne} \rangle$, open symbols the HICO regime, and lines are different values of the D_2 throughput (corresponding to figure 17).

When starting in the Conventional Regime, the effect of increasing Γ_{Ne} is to simultaneously reduce the temperature of both divertors and $n_{e,sep}^{OMP}$. At a threshold level of Γ_{Ne}, the solution transitions to the HICO regime, indicated by the open symbols. When the solution is already in the HICO or HOCI regime, the addition of Γ_{Ne} further increases the level of asymmetry between the divertors.

The solid black trace shows a time-dependent simulation where Γ_{Ne} was increased from 0 to 1.8 $\times 10^{20}$ atoms s^{-1} over 0.5 s starting from a main ion throughput of $\Gamma_{D2} = 2 \times 10^{22}$ atoms s^{-1}. It can be seen that the time-dependent simulation reproduces the general trend of the steady-state runs, however a slower ramp may be required to accurately match the results.

The reduction in $n_{e,sep}^{OMP}$ with increasing impurity concentration is typically observed in SOLPS simulations [17, 39, 64]. This effect can be understood as 'power limitation' or 'power starvation', where volumetric power and momentum sinks lead to a reduction in the divertor recycling flux (and T_e). This effect can be complex (see e.g. discussion in [65, 66]), but a simple picture (neglecting recombination) is that for fixed upstream $q_{||u}$ an increase in P_{rad} will cause a drop in $\Gamma_{||t}(\gamma T_e + \epsilon)$, where γ is the sheath heat transmission coefficient and ϵ is the energy loss per ionization.

The reduction in $n_{e,sep}^{OMP}$ and the integrated ion flux to the divertors as a function of Γ_{Ne} is shown in figure 18 panels (*c*)–(*e*). The increasing $\langle c_{Ne} \rangle$, separatrix neon density, and radiated power in each divertor volume are shown in panels (*a*) and (*b*)–(*f*), respectively. The radiated power is approximately evenly distributed between the outer and inner divertors

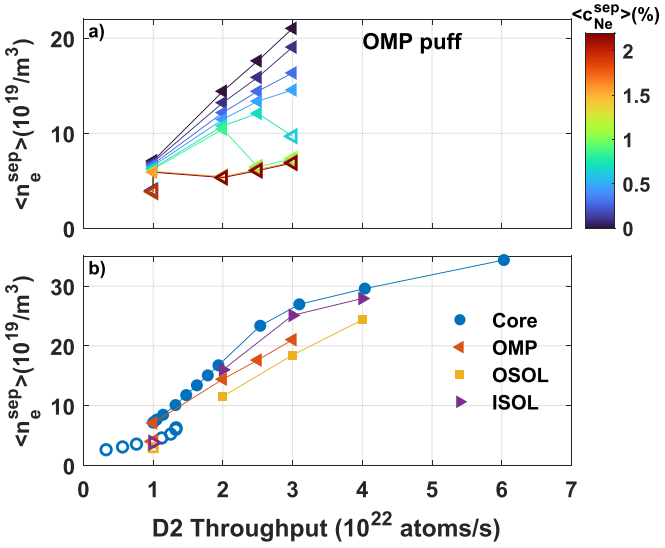

Figure 19. Averaged upstream separatrix electron density as a function of D_2 throughput for (*a*) OMP puff at several levels of $\langle c_{\mathrm{Ne}} \rangle$ and (*b*) different puff locations without neon seeding with $P_{\mathrm{SOL}} = 10$ MW. Open symbols indicate solutions in the HICO regime.

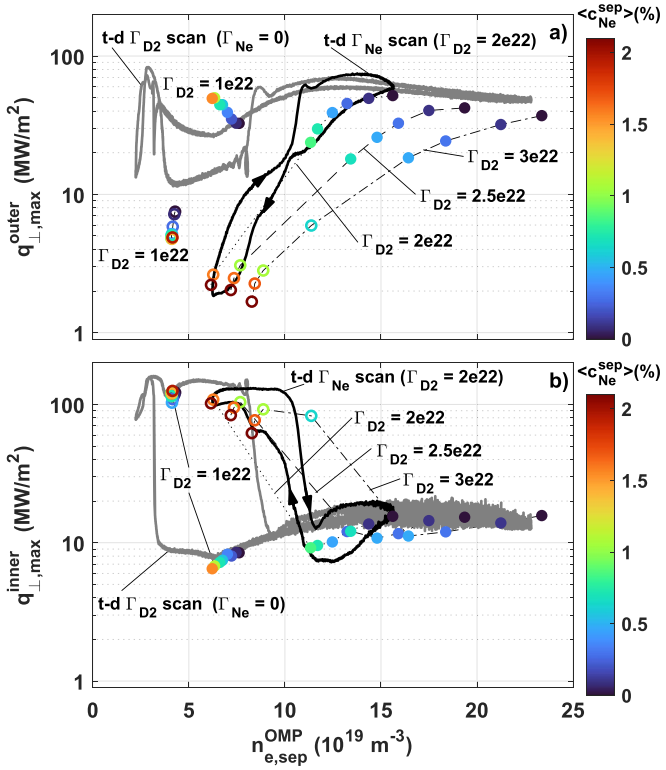

Figure 20. Peak total energy flux to the (*a*) outer and (*b*) inner divertor as a function of the upstream density, main ion throughput and neon concentration $\langle c_{\mathrm{Ne}} \rangle$ with $P_{\mathrm{SOL}} = 10$ MW. Peak fluxes below 30 MW m^{-2} can be achieved for $\Gamma_{D2} > 2 \times 10^{22}$ and $\Gamma_{\mathrm{Ne}} > 8 \times 10^{20}$ atoms s^{-1}, although additional Γ_{Ne} results in a back-transition to the HICO regime. The inner divertor peak flux is below 20 MW m^{-2} for all non-HICO solutions. Arrows indicate direction of time in seeding scan.

(corresponding to the yellow and purple regions in figure 1). As P_{rad} increases, the recycling flux and $n_{\mathrm{e,sep}}^{\mathrm{OMP}}$ drop. The neon throughput Γ_{Ne} appears to be a somewhat better sorting parameter than $\langle c_{\mathrm{Ne}} \rangle$ for the value of P_{rad}. After the back transition to the HICO regime (indicated by open symbols), the inner divertor recycling flux is strongly reduced and the radiated power from both divertor volumes drops as neither have the T_{e} distribution for effective neon radiation.

To find a operating regime where the divertor conditions are acceptable and $n_{\mathrm{e,sep}}^{\mathrm{OMP}}$ matches a core scenario, the main ion fueling should be increased to counteract the drop in $n_{\mathrm{e,sep}}^{\mathrm{OMP}}$ with Γ_{Ne}. Over the range of Γ_{D2} scanned, the upstream density increases with Γ_{D2}, both for fixed values of Γ_{Ne} (unless a back-transition to HICO occurs) and without neon seeding for several D_2 puff locations, see figures 19*(a)* and *(b)*. A separatrix averaged value of $n_{\mathrm{e,sep}}^{\mathrm{OMP}}$ is used to avoid bias due to local sourcing in the case of an OMP puff. This is in contrast to SOLPS simulations of ITER, where the upstream density 'clamps' at a certain throughput level and no longer increases with Γ_{D2} [17]. At the highest levels of D_2 throughput, the fueling efficiency is reduced, however no saturated level is found over the explored range. The differences in the ITER and SPARC simulations in this respect may be due to the size of the device relative to the ionization mean free paths, or 'clamping' might be observed at higher Γ_{D2} in SPARC, but this relative difference has not been explored in detail at this time.

Figure 20 shows the peak total flux to the *(a)* outer and *(b)* inner divertor for a range of Γ_{D2} and Γ_{Ne} throughput levels. For the steady-state simulations (symbols) the energy flux includes contributions from the plasma, neutral particles and radiation, while for the time-dependent simulations neutral particles (including reflected power) and radiation are neglected due to reduced code output. Taking 30 MW m^{-2} as a rough estimate for an upper limit for acceptable steady-state conditions with strike-point sweeping, solutions are found for $\Gamma_{D2} > 2 \times 10^{22}$ and $\Gamma_{\mathrm{Ne}} > 8 \times 10^{20}$ atoms s^{-1}. These solutions are somewhat marginal, however, as a further increase in Γ_{Ne} is predicted to cause a back-transition to the HICO regime. Figure 20 suggests that a further increase in Γ_{D2} should move to a more stable operational regime (without back-transition). These scenarios will have to be carefully evaluated with respect to the upstream values of $n_{\mathrm{e,sep}}^{\mathrm{OMP}}$ and $\langle c_{\mathrm{Ne}} \rangle$ to determine if they are compatible with the core scenario. This highlights the multiple input multiple output (MIMO) nature of the control problem, as recently demonstrated on TCV [67]. Further increasing the input power to 29 MW will increase the seeding requirements, to be explored further in a future publication.

The components of the divertor energy fluxes are shown in figures 21 and 22 for the outer and inner targets, respectively, for $\Gamma_{D2} = 2.5 \times 10^{22}$ atoms s^{-1}. The top panels show the composition into loads due to radiation, neutral particles, and plasma particles for $\Gamma_{\mathrm{Ne}} = 0$ ($\langle c_{\mathrm{Ne}} \rangle = 0\%$) and $\Gamma_{\mathrm{Ne}} = 1.1 \times 10^{20}$ atoms s^{-1} ($\langle c_{\mathrm{Ne}} \rangle = 0.8\%$). The outer divertor is dominated by plasma loads, while the inner divertor has a significant load due to incident neutral particles near the strike

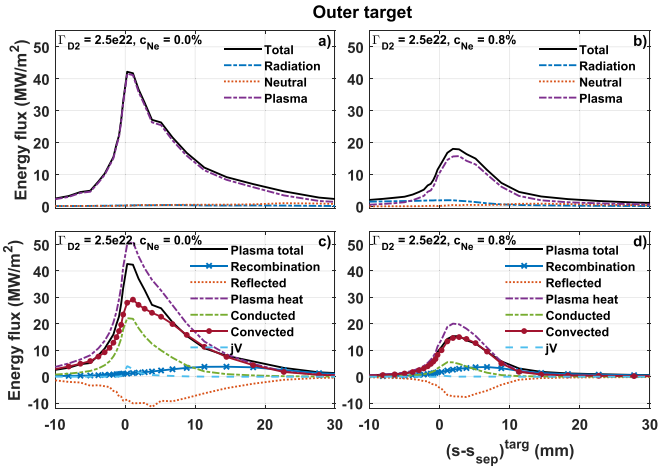

Figure 21. Components of the outer divertor total energy flux with $\Gamma_{D2} = 2.5 \times 10^{22}$ atoms s^{-1} and (*a*) $\langle c_{\rm Ne} \rangle = 0\%$ and (*b*) $\langle c_{\rm Ne} \rangle = 0.8\%$. The total plasma flux is further separated into contributions from surface recombination, plasma heat flux (further decomposed into conduction and convection), and the reflection of incident ions into neutral atoms and molecules in panels (*c*) and (*d*).

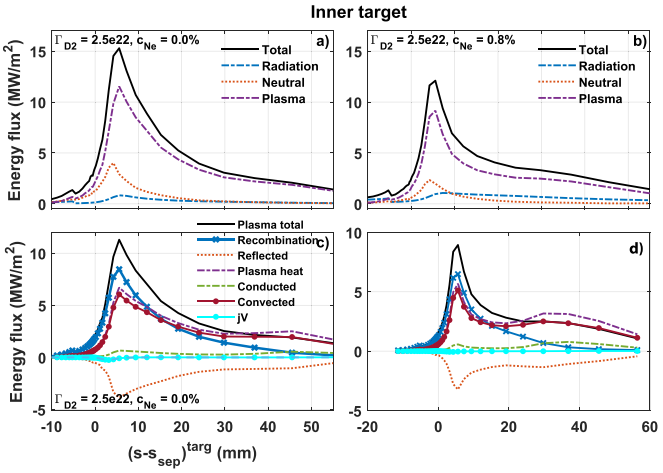

Figure 22. Components of the inner divertor total energy flux with $\Gamma_{D2} = 2.5 \times 10^{-22}$ atoms s^{-1} and (*a*) $\langle c_{\rm Ne} \rangle = 0\%$ and (*b*) $\langle c_{\rm Ne} \rangle = 0.8\%$. The total plasma flux is further separated into contributions from surface recombination, plasma heat flux (further decomposed into conduction and convection), and the reflection of incident ions into neutral atoms and molecules in panels (*c*) and (*d*).

point. The radiated power flux is ≈1–2 MW m^{-2} on both targets when $\langle c_{\rm Ne} \rangle = 0.8\%$. The bottom panels breaks the incident plasma flux into contributions from surface recombination, plasma heat flux (further decomposed into conduction and convection), and the reflection of incident ions into neutral atoms and molecules. The outer target has a significant contribution due to conduction and convection, while the inner target plasma flux is predominantly from surface recombination and convection due to the relatively higher degree of detachment.

5. Conclusions

Operation of the SPARC divertor has been explored numerically using the SOLPS-ITER code for a range of code inputs including cross-field diffusivities, power crossing the separatrix, main ion throughput, neon impurity seeding level, and gas puff locations. Without impurity seeding, for conservative values of cross-field diffusivities leading to $\lambda_q \approx 0.14$ mm, the conditions on the outer divertor at an steady-state upstream electron density of 1×10^{-20} m^{-3} are predicted to be extreme due to the compact size of SPARC. With $P_{\rm SOL} = 10$ MW, the peak divertor heat fluxes may be at the maximum acceptable range to exhaust with strike-point sweeping, although the high $T_{\rm e}$ may lead to a significant tungsten source which would limit the maximum pulse length. At $P_{\rm SOL} = 29$ MW, further dissipation with impurity seeding is likely to be required.

Increasing the simulated λ_q to 0.3 mm or larger significantly eases the divertor challenge, either in terms of the necessary impurity radiation at high $P_{\rm SOL}$ or the frequency of strike-point sweeps at lower power. Operation in a double null topology could further reduce the outer divertor fluxes, although this scenario was not explored here.

Density scans reveal a region of $n_{\rm e,sep}^{\rm OMP}$ with multiple solutions where the divertor solutions have extreme asymmetry in $T_{\rm e}$, $n_{\rm e}$ and deposited heat flux. The solutions, labeled here as 'Hot Inner Cold Outer' and 'Hot Outer Cold Inner', exhibit hysteresis, with the steady-state value depending on the initial condition. The asymmetry is due to a thermodynamic instability, where a parallel temperature gradient along a SOL flux tube results in a parallel current driven heat flux from the cold to the hot divertor. This instability, driven by thermoelectric currents, has been observed previously in simulation and experiment, but is particularly significant in SPARC due to the extreme values of predicted divertor $T_{\rm e}$ at low values of λ_q. The magnitude and density window of the hysteresis region is reduced with larger λ_q or by introducing impurities, although it is present in some degree in each case. Time-dependent simulations indicate a rapid transition between these regimes.

In this respect we note an interesting aspect of the presented modelling cases. Some simulations are performed with λ_q in the range as predicted both by the HD model of Goldston [68] and empirically by Reg.#9 in [4]. The latter representing JET, ASDEX Upgrade, DIII-D and C-Mod, all having the same aspect ratio as SPARC. This empirical interpretation results in a power width of about 0.5 mm for low density cases (see figure 3) and correspond to $\chi_\perp = 0.1\,{\rm m}^2\,{\rm s}^{-1}$. The observed bifurcation from or to HOCI and HICO were not observed in experiments serving for the data base in [4] . This is important to note because the edge densities for which HOCI/HICO are observed in the simulation are significantly below the ones reported for type-I ELMy H-Mode conditions in terms of Greenwald.

The existence of the hysteresis region at low $n_{\rm e,sep}^{\rm OMP}$ does not necessarily present an issue for steady-state SPARC operation, however it may introduce additional complexity into the system for divertor condition control. This is particularly evident when impurity seeding is added. When introduced from

the Conventional regime (where thermoelectric currents and asymmetry are small), the peak divertor fluxes are dissipated due to impurity radiation, but the upstream density drops due to a reduction in the recycling flux (power limitation or power starvation). If the upstream density drops below a threshold value, a back transition to the 'Hot Inner Cold Outer' regime occurs. Increasing the main ion throughput counteracts the upstream density drop, albeit at the potential additional complexity of a MIMO control strategy. Over the range of main ion throughput evaluated here, Γ_{D2} remains an effective actuator for controlling $n_{e,sep}^{OMP}$, with no indication of saturation as observed in SOLPS simulations of ITER.

There are several important caveats when using these SOLPS simulations to inform SPARC operation. No simulations here include cross-field plasma drifts, which are known to be important to predict the divertor conditions in present devices. Furthermore, drift effects at the separatrix are reported to effect the minimum SOL power width (at lowest densities) and may lead to steady state situation less prone to the described bifurcated scenarios [69, 70]. Further, the inclusion of drifts may have a significant effect on the details of the parallel current profile and therefore the hysteresis and asymmetric effects described in this paper. Only a single magnetic topology and PFC geometry was considered. Operation with a vertical outer target configuration may affect the simulation state globally. There is also significant uncertainty in the cross-field transport coefficients, which was only investigated over a small range in this paper. Efforts by the global SOLPS community (and other boundary codes) have indicated areas for possible improvement of the physics model, in terms of plasma-neutral reaction descriptions and plasma-surface interaction effects enabled by a full grid of the plasma transport domain to the first wall. Despite these caveats, the SOLPS solutions should serve as a investigation into the plasma boundary physics that can be expected in SPARC, and used to inform the operational scenarios and control strategies, including actuation and sensing.

Acknowledgments

This manuscript has been authored by UT-Battelle, LLC, with the US Department of Energy (DOE). The work was supported in part by the US DOE Office of Fusion Energy Sciences under Contract DE-AC05-00OR22725 under the spherical tokamak program, by the ORNL Laboratory Directed Research and Development Program, by the Innovation Network for Fusion Energy (INFUSE), and by Commonwealth Fusion Systems. This research used resources of the Oak Ridge National Laboratory Research Cloud. The results are obtained with the help of the EIRENE package (see www.eirene.de) including the related code, data and tools [22].

ORCID iDs

Jeremy D. Lore https://orcid.org/0000-0002-9192-465X
Jae-Sun Park https://orcid.org/0000-0003-0871-7527
Thomas Eich https://orcid.org/0000-0003-3065-8420
Adam Q. Kuang https://orcid.org/0000-0002-8917-2911
Matthew L. Reinke https://orcid.org/0000-0003-4413-9613
Sebastian De Pascuale https://orcid.org/0000-0001-7142-0246
Bart Lomanowski https://orcid.org/0000-0003-2226-2004
Alex Creely https://orcid.org/0000-0002-4464-150X
John M. Canik https://orcid.org/0000-0001-6934-6681

References

[1] Creely A., Greenwald M.J., Ballinger S.B., Brunner D., Canik J., Doody J., Fülöp T., Garnier D., Granetz R. and Gray T. 2020 *J. Plasma Phys.* **86** 865860502
[2] Creely A.J., Brunner D., Mumgaard R.T., Reinke M.L., Segal M., Sorbom B.N. and Greenwald M.J. 2023 *Phys. Plasmas* **30** 090601
[3] Kuang A., Ballinger S., Brunner D., Canik J., Creely A., Gray T., Greenwald M., Hughes J., Irby J. and LaBombard B. 2020 *J. Plasma Phys.* **86** 865860505
[4] Eich T. *et al* (ASDEX Upgrade Team1 and JET EFDA Contributors) 2013 *Nucl. Fusion* **53** 093031
[5] Brunner D., LaBombard B., Kuang A. and Terry J. 2018 *Nucl. Fusion* **58** 094002
[6] Goldston R.J., Reinke M.L. and Schwartz J.A. 2017 *Plasma Phys. Control. Fusion* **59** 055015
[7] Chang C. *et al* 2017 *Nucl. Fusion* **57** 116023
[8] Xu X., Li N., Li Z., Chen B., Xia T., Tang T., Zhu B. and Chan V. 2019 *Nucl. Fusion* **59** 126039
[9] Ernst D.R. *et al* 2024 *Phys. Rev. Lett.* **132** 235102
[10] Li Z. *et al* 2024 *Commun. Phys.* **7** 2399–3650
[11] Cowley C., Kuang A.Q., Moulton D., Lore J.D., Canik J., Umansky M., Wigram M., Ballinger S., Lipschultz B. and Bonnin X. 2023 *Plasma Phys. Control. Fusion* **65** 035011
[12] Wiesen S., Reiter D., Kotov V., Baelmans M., Dekeyser W., Kukushkin A., Lisgo S., Pitts R., Rozhansky V. and Saibene G. 2015 *J. Nucl. Mater.* **463** 480–4
[13] Rognlien T., Milovich J., Rensink M. and Porter G. 1992 *J. Nucl. Mater.* **196–198** 347–51
[14] Ballinger S., Kuang A.Q., Umansky M., Brunner D., Canik J.M., Greenwald M., Lore J.D., LaBombard B., Terry J.L. and Wigram M. 2021 *Nucl. Fusion* **61** 086014
[15] Park J.S., Lore J.D., Reinke M., Kuang A.Q., Pascuale S.D. and Creely A. 2024 *Nucl. Fusion* **64** 076036
[16] Kukushkin A., Pacher H., Kotov V., Pacher G. and Reiter D. 2011 *Fusion Eng. Des.* **86** 2865–73
[17] Pitts R. *et al* 2019 *Nucl. Mater. Energy* **20** 100696
[18] Lore J., Pascuale S.D., Laiu P., Russo B., Park J.S., Park J., Brunton S., Kutz J. and Kaptanoglu A. 2023 *Nucl. Fusion* **63** 046015
[19] Park J.-S., Pitts R., Jang J., Han Y.S., Choe W., Lore J., Hwang J., Bak J.-G., Juhn J.-W. and Hong S.-H. 2023 *Nucl. Fusion* **63** 086018
[20] Looby T., Reinke M., Wingen A., Menard J., Gerhardt S., Gray T., Donovan D., Unterberg E., Klabacha J. and Messineo M. 2022 *Fusion Sci. Technol.* **78** 10–27
[21] Bonnin X., Dekeyser W., Pitts R., Coster D., Voskoboynikov S. and Wiesen S. 2016 *Plasma Fusion Res.* **11** 1403102
[22] Reiter D., Baelmans M. and Börner P. 2005 *Fusion Sci. Technol.* **47** 172–86
[23] Boeyaert D., Carli S., Dekeyser W., Wiesen S. and Baelmans M. 2024 *Phys. Plasmas* **31** 023905
[24] Braginskii S. 1965 *Rev. Plasma Phys.* **1** 205

[25] Balescu R. 1988 *Transport Processes in Plasmas* (*Transport Processes in Plasmas* no pt. 2) (North-Holland)
[26] Schneider R., Bonnin X., Borrass K., Coster D.P., Kastelewicz H., Reiter D., Rozhansky V.A. and Braams B.J. 2006 *Contrib. Plasma Phys.* **46** 3–191
[27] Chankin A.V. *et al* 2006 *Plasma Phys. Control. Fusion* **48** 839
[28] Chen Y., Zhang D., Liu S., Xu G., Wang L., Yao D., Luo Z., Hu L. and Team E. 2020 *Nucl. Fusion* **60** 036019
[29] Hitzler F., Wischmeier M., Reimold F. and Coster D.P. (the ASDEX Upgrade Team) 2020 *Plasma Phys. Control. Fusion* **62** 085013
[30] Reimold F. *et al* 2015 *J. Nucl. Mater.* **463** 128–34
[31] Rognlien T., Umansky M., Xu X., Cohen R. and LoDestro L. 2005 *J. Nucl. Mater.* **337–339** 327–31
[32] Zhang D., Chen Y., Xu X., Xia T. and Liu S. team E 2020 *Nucl. Fusion* **60** 106015
[33] Bufferand H. *et al* 2016 *Contrib. Plasma Phys.* **56** 555–62
[34] Carli S., Dekeyser W., Coosemans R., Dejarnac R., Komm M., Dimitrova M., Adámek J., Bílková P. and Böhm P. 2020 *Contrib. Plasma Phys.* **60** e201900155
[35] Dekeyser W., Coosemans R., Carli S. and Baelmans M. 2022 *Contrib. Plasma Phys.* **62** e202100190
[36] Rodriguez-Fernandez P., Creely A., Greenwald M., Brunner D., Ballinger S., Chrobak C., Garnier D., Granetz R., Hartwig Z. and Howard N. 2022 *Nucl. Fusion* **62** 042003
[37] Rodriguez-Fernandez P., Howard N. and Candy J. 2022 *Nucl. Fusion* **62** 076036
[38] Hughes J.W., Howard N.T., Rodriguez-Fernandez P., Creely A.J., Kuang A.Q., Snyder P.B., Wilks T.M., Sweeney R. and Greenwald M. 2020 *J. Plasma Phys.* **86** 865860504
[39] Lore J., Bonnin X., Park J.S., Pitts R. and Stangeby P. 2022 *Nucl. Fusion* **62** 106017
[40] Rodriguez-Fernandez P., Howard N.T., Greenwald M.J., Creely A.J., Hughes J.W., Wright J.C., Holland C., Lin Y. and Sciortino F. 2020 *J. Plasma Phys.* **86** 865860503
[41] Stangeby P., Lore J., Pitts R., Canik J. and Bonnin X. 2022 *Nucl. Fusion* **63** 016017
[42] Du H., Zheng G., Bonnin X., Li J., Xue L., Duan X. and Huang W. 2020 *Nucl. Mater. Energy* **22** 100719
[43] Du H., Sang C., Wang L., Bonnin X., Sun J. and Wang D. 2014 *Fusion Eng. Des.* **89** 2461–6
[44] Lasa A. *et al* 2024 *Nucl. Fusion* **64** 076006
[45] Bonnin X., Pitts R., Komarov V., Escourbiac F., Merola M., Bo L., Wei L., Pan L. and Kukushkin A. 2017 *Nucl. Mater. Energy* **12** 1100–5
[46] Sang C., Du H., Zuo G., Bonnin X., Sun J., Wang L. and Wang D. 2016 *Nucl. Fusion* **56** 106018
[47] Hinton F. 1983 *Collisional Transport in Plasma* (Fusion Research Center)
[48] Rozhansky V., Kaveeva E., Voskoboynikov S., Coster D., Bonnin X. and Schneider R. 2003 *Nucl. Fusion* **43** 614
[49] Meier E.T., Goldston R.J., Kaveeva E.G., Makowski M.A., Mordijck S., Rozhansky V.A., Senichenkov I.Y. and Voskoboynikov S.P. 2016 *Plasma Phys. Control. Fusion* **58** 125012
[50] Orrico C., Ravensbergen T., Pitts R., Bonnin X., Kaveeva E., Park J., Rozhansky V., Senichenkov I., Watts C. and de Baar M. 2023 *Nucl. Fusion* **63** 086002
[51] Hayashi N., Takizuka T., Hatayama A. and Ogasawara M. 1999 *J. Nucl. Mater.* **266–269** 526–31
[52] Labombard B. *et al* 1997 *J. Nucl. Mater.* **241–243** 149–66
[53] Harbour P. *et al* 1989 *J. Nucl. Mater.* **162–164** 236–44
[54] Kallenbach A., Carlson A., Pautasso G., Peeters A., Seidel U. and Zehrfeld H.P. 2001 *J. Nucl. Mater.* **290–293** 639–43
[55] Brida D., Silvagni D., Eich T., Faitsch M. and McCarthy P. (the ASDEX Upgrade Team and the MST1 Team) 2020 *Plasma Phys. Control. Fusion* **62** 105014
[56] Staebler G. and Hinton F. 1989 *Nucl. Fusion* **29** 1820
[57] Staebler G. 1996 *Nucl. Fusion* **36** 1437
[58] Rozhansky V.A., Shirobokov A.A. and Kaveeva E.G. 2024 *Contrib. Plasma Phys.* **64** e202300122
[59] Kukushkin A.S. and Krasheninnikov S.I. 2019 *Plasma Phys. Control. Fusion* **61** 074001
[60] Wigram M., LaBombard B., Umansky M., Kuang A., Golfinopoulos T., Terry J., Brunner D., Rensink M., Ridgers C. and Whyte D. 2019 *Nucl. Fusion* **59** 106052
[61] Balbinot L., Rubino G. and Innocente P. 2021 *Nucl. Mater. Energy* **27** 100952
[62] Islam M.S., Lore J.D., Lau C. and Rapp J. 2023 *Plasma Phys. Control. Fusion* **65** 095020
[63] Park J.S., Bonnin X., Pitts R. and Lore J. 2024 *Nucl. Fusion* **64** 036002
[64] Islam M., Lore J., Smolentsev S., Kessel C. and Maingi R. 2024 *Nucl. Fusion* **64** 056036
[65] Stangeby P.C. 2018 *Plasma Phys. Control. Fusion* **60** 044022
[66] Krasheninnikov S. and Kukushkin A.S. 2022 *Phys. Plasmas* **29** 122502
[67] Koenders J., Perek A., Galperti C., Duval B., Février O., Theiler C. and van Berkel M. (the TCV Team) 2023 *Nucl. Fusion* **63** 106007
[68] Goldston R. 2011 *Nucl. Fusion* **52** 013009
[69] Reiser D. and Eich T. 2017 *Nucl. Fusion* **57** 046011
[70] Meier E., Goldston R., Kaveeva E., Makowski M., Mordijck S., Rozhansky V., Senichenkov I. and Voskoboynikov S. 2017 *Nucl. Mater. Energy* **12** 973–7